Surface Composition and Enrichment Effects in Mixtures of Functionalized and Non-Functionalized Ionic Liquids

Oberflächenzusammensetzung und Anreicherungseffekte
in Mischungen funktionalisierter und
nicht-funktionalisierter Ionischer Flüssigkeiten

Der Naturwissenschaftlichen Fakultät
der Friedrich-Alexander-Universität Erlangen-Nürnberg

zur Erlangung des Doktorgrades Dr. rer. nat.

vorgelegt von

BETTINA HELLER
aus Erlangen

Als Dissertation genehmigt von der Naturwissenschaftlichen Fakultät
der Friedrich-Alexander-Universität Erlangen-Nürnberg

Tag der mündlichen Prüfung: 25.05.2020

Vorsitzender des Promotionsorgans: Prof. Dr. Georg Kreimer

Gutachter: Prof. Dr. Hans-Peter Steinrück

                                     Prof. Dr. Jürgen Schatz

Table of Contents

Published Papers

[P1] **Probing the Surface Tension of Ionic Liquids Using the Langmuir Principle**

K. Shimizu, <u>B. S. J. Heller</u>, F. Maier, H.-P. Steinrück, J. N. Canongia Lopes

Langmuir **2018**, *34*, 4408–4416.

The author's contribution is the ARXPS data analysis and interpretation.

[P2] **Surface Enrichment in Equimolar Mixtures of Non-Functionalized and Functionalized Imidazolium-Based Ionic Liquids**

<u>B. S. J. Heller</u>, C. Kolbeck, I. Niedermaier, S. Dommer, J. Schatz, P. Hunt, F. Maier, H.-P. Steinrück

ChemPhysChem **2018**, *19*, 1733–1745.

The author's contribution is the sample preparation, ARXPS investigation, data analysis, data interpretation and manuscript preparation.

[P3] **Temperature-Dependent Surface Enrichment Effects in Binary Mixtures of Fluorinated and Non-Fluorinated Ionic Liquids**

<u>B. S. J. Heller</u>, M. Lexow, F. Greco, S. Shin, G. Partl, F. Maier, H.-P. Steinrück

Chem. Eur. J. **2020**, *26*, 1117–1126.

The author's contribution is the sample preparation, ARXPS investigation, data analysis, data interpretation and manuscript preparation.

[P4] **Pronounced surface enrichment of fluorinated ionic liquids in binary mixtures with methoxy-functionalized ionic liquids**

<u>B. S. J. Heller</u>, U. Paap, F. Maier, H.-P. Steinrück

J. Mol. Liq. **2020**, *305*, 112783.

The author's contribution is the sample preparation, ARXPS investigation, data analysis, data interpretation and manuscript preparation.

[P5] **Few layer 2D pnictogens catalyze the alkylation of soft nucleophiles with esters**

V. Lloret, M. Á. Rivero-Crespo, J. A. Vidal-Moya, S. Wild, A. Doménech-Carbó, <u>B. S. J. Heller</u>, S. Shin, H.-P. Steinrück, F. Maier, F. Hauke, M. Varela, A. Hirsch, A. Leyva-Pérez, G. Abellán

Nat. Commun. **2019**, *10*, 509.

The author's contribution is the XPS investigation, data analysis and interpretation.

1   Introduction

Ionic liquids (ILs) are salt melts with melting points typically below 100 °C, often even below room temperature. They are composed of organic cations and organic or inorganic anions, allowing for a wide structural variability including functional groups with hetero-atoms, branched chains or aromatic groups.[1-4] The structural diversity results in a great tunability of physical and chemical properties like thermal stability, ionic conductivity, vis-cosity, solubility and electrochemical window, to name a few.[5-7] By mixing ILs in different compositions (note that the term "IL" is used throughout this thesis for neat ILs consisting of only one type of cation and anion), further fine tuning of properties is possible.[8-11] Thus, ILs and their mixtures are promising candidates for a range of applications in the field of *e.g.* electrochemistry,[5, 12-22] lubrication,[6, 23] extrac-tion[5, 19, 24-30] and catalysis.[1, 7, 31-36]

In many of these applications, the outer surface representing the interface of the IL phase with the gas phase plays a major role. This is particularly true for large surface area systems like the Supported Ionic Liquid Phase (SILP)[36-39] catalysis. In SILP, a porous high surface area support is coated with a thin IL film, which contains the homogeneously dissolved catalyst. Gaseous reactants and the reaction products have to pass through the IL surface layer, which – in comparison to the isotropic bulk environment – can be very different in terms of composition and molecular orientation. Moreover, functionalized groups present in the IL can also have a profound impact on the composition of the topmost layer.[8, 9, 36, 40-57]

Therefore, a better understanding of the surface of neat ILs and of IL mixtures is of great interest. During the last two decades, the knowledge about the surface of ILs and IL mixtures has been extended using different surface-sensitive techniques such as small-angle X-ray and neutron scattering,[8] X-ray reflectivity,[58] low-energy ion scattering (LEIS),[46, 59] reactive-atom scattering with laser-induced fluorescence detection (RAS-LIF),[8, 60] time-of-flight secondary ion mass spectrometry (TOF-SIMS),[50, 61] metastable induced electron spectroscopy (MIES),[57, 62] Rutherford backscattering spectroscopy (RBS),[50, 51, 63, 64] X-ray photoelectron spectroscopy (XPS)[52-54, 62, 65-69] and simula-tions.[2, 8, 54-56, 60, 64, 70-72] The extremely low vapor pressure of most ILs makes them suitable for investigations under ultra-high vacuum (UHV) conditions, which is required for some of the aforementioned techniques.

As will be demonstrated in this work, angle-resolved XPS (ARXPS) allows one to gain detailed information about the bulk and surface composition of IL systems by comparing spectra recorded under $0°$ and $80°$ emission (see Chapter 2). All ILs and their mixtures investigated here are based on imidazolium cations that contain alkyl chains or functional groups such as methoxy or fluorinated moieties (see Chapter 3). In Chapter 4.1, the surface enrichment of the alkyl chains of $[C_nC_1Im][Tf_2N]$ (with $n = 2, 4, 6, 8, 10$ and 12) with respect to the cationic head groups is correlated to the surface tension values of the ILs. The study of the IL/vacuum interface as well as the bulk composition of neat ILs and binary IL mixtures of a functionalized and a non-functionalized IL or two functionalized ILs are presented in Chapters 4.2.1 to 4.2.3: Surface enrichment and depletion effects in mixtures of $[C_8C_1Im][PF_6]$ or $[C_8C_1Im][Tf_2N]$ with $[(MeO)_2Im][PF_6]$ are investigated. Furthermore, mixtures containing $[PFBMIm][PF_6]$ and $[C_nC_1Im][PF_6]$ with $n = 2, 4$ and 8 and mixtures of $[(MeO)_2Im][PF_6]$ and $[PFBMIm][PF_6]$ are studied by temperature-dependent ARXPS from $95\,°C$ to their onset of solidification. This gives crucial information for SILP systems since the temperature of the process might have a major impact on the surface composition; for some reactions, *e.g.* the exothermal water-gas shift reaction, a lower temperature is desirable.[73]

Finally, in Chapter 4.3, the role of $[C_4C_1Im][BF_4]$ as dispersing and stabilizing solvent to produce the catalytically active two-dimensional (2D) materials antimonene and phosphorene is discussed, particularly with respect to the protection of these pnictogens against oxidation under ambient conditions.

2 Angle-Resolved X-ray Photoelectron Spectroscopy

X-ray photoelectron spectroscopy (XPS) is an ultra-high vacuum (UHV)-based surface science technique, which was used to perform the experiments presented in this thesis. In this chapter, the basic aspects of XPS are highlighted. For more details, see *e.g.* the books of van der Heide,[74] Briggs and Seah[75] or Hüfner.[76]

XPS is based on the photoelectric effect which was first described by Hertz[77] and Hallwachs[78] in 1887 and 1888 and explained by Einstein in 1905.[79] A general scheme is shown in Figure 2.1.
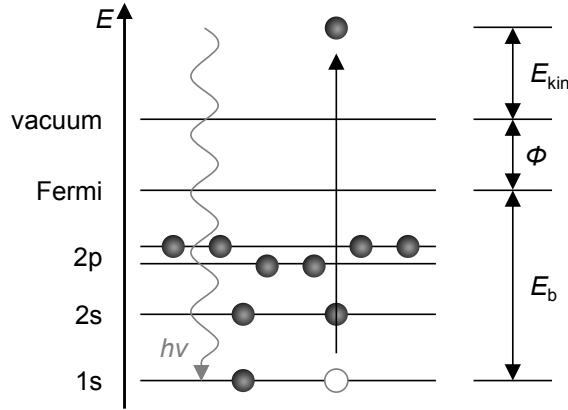
Figure 2.1: General scheme of the photoelectric effect.

A sample is irradiated by photons of a fixed energy, $h\nu$, and photoelectrons with different kinetic energies are emitted from the core levels to above the sample vacuum level, E_{vacuum}. These photoelectrons are then detected by an electron analyzer. Their kinetic energy, E_{kin}, is measured with respect to the vacuum level of the analyzer, $E_{vacuum,an}$. Taking the work function of the analyzer, Φ_{an}, into account, which is a constant derived by calibrating the analyzer to the Fermi level, E_{Fermi}, of a clean metal sample, the binding energy, E_b, of the excited orbital with respect to the common E_{Fermi}, can be obtained:

$$E_b = h\nu - E_{kin} - \Phi_{an} \tag{1}$$

Note that this relation holds only for conducting samples electrically connected to the electron analyzer ground to align E_{Fermi} of both sample and analyzer.

The binding energy of the detected electrons is element specific and allows for extracting information on the chemical environment and oxidation state of the probed atom by the so-called chemical shifts. XPS is thus also known as Electron Spectroscopy for

Chemical Analysis (ESCA). Moreover, XPS is a quantitative technique to extract the composition of a sample by the signal intensities (apart from hydrogen and helium).

XPS is a very surface-sensitive method resulting from the short inelastic mean free path, λ, of the excited photoelectrons in matter. This surface sensitivity is characterized by the so-called information depth, ID, which is also denoted as sample depth or escape depth. The ID depends on the emission angle, ϑ, of the photoelectrons relative to the surface normal (see Figure 2.2), and is defined as:

$$ID\,(\vartheta) = 3\lambda \cdot cos\,\vartheta \qquad (2)$$

It corresponds to the depth, where 96% of the measured XP signal originates from.[74] For $\vartheta = 0°$, the ID is 7 to 9 nm, depending on E_{kin}. Increasing ϑ results in a decreased ID according to Equation 2: For measurements at $\vartheta = 80°$, as performed in the course of this thesis, ID is only 1 to 1.5 nm, which limits the detected signal mostly to the topmost surface layer of the studied ILs.
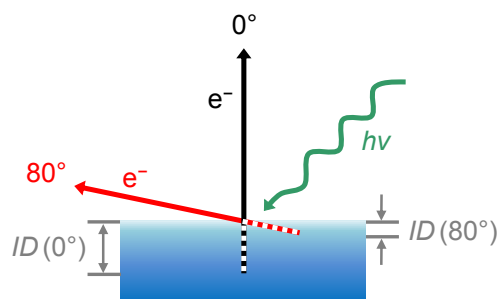
Figure 2.2: Scheme of ARXPS recorded under $\vartheta = 0°$ and 80° emission with respect to the surface normal of the sample. The dashed lines indicate the maximum "traveled" distance of 3λ of electrons in matter at both emission angles; the resulting information depth, ID, is marked in gray.

At a given emission angle, the intensity, I_d, of a signal originating from a depth, d, relative to the intensity, I_0, at the IL/vacuum interface ($d = 0$) decays exponentially according to:[80]

$$\frac{I_d}{I_0} = e^{-\frac{d}{\lambda\cdot cos\,\vartheta}} \qquad (3)$$

Figure 2.3 highlights the dependence of the surface sensitivity of angle-resolved XPS (ARXPS) on the emission angle. The exponential decay of the contribution to the measured XP signal is illustrated in Figure 2.3–right for 0° (black) and 80° (red) emission and a scaled molecular dynamics (MD) simulation of the near-surface region of [C$_8$C$_1$Im][Tf$_2$N] is shown in Figure 2.3–left. For both emission angles, the behavior is

shown for photoelectrons excited from distinct core levels (F 1s, N 1s and P 2p) with different E_b and thus different E_{kin} and λ values ($\lambda_{F\ 1s} = 2.0$ nm, $\lambda_{N\ 1s} = 2.5$ nm, $\lambda_{P\ 2p} = 3.0$ nm; linearly[81] interpolated from previously published values[40, 80, 82-84]). In 80° emission, 86% of the signal of the N 1s core level originates from the first IL double layer ($d = 0.84$ nm), whereas in 0° it is only 29%. These values differ depending on λ of the photoelectrons with different E_{kin} as indicated by the solid (F 1s), dashed (N 1s) and dotted (P 2p) lines in Figure 2.3–right.

Figure 2.3: Side view of a scaled MD simulation of [C₈C₁Im][Tf₂N] (left).[85] Exponential decay of the contribution of individual [C₈C₁Im][Tf₂N] double layers to the overall ARXPS signal in the F 1s (solid), N 1s (dashed) and P 2p (dotted) spectra under 0° (black) and 80° (red) emission (right). The mean ion pair size is estimated from the third root of the molecular volume, V_m.[80, 86] λ is 2.0, 2.5 and 3.0 nm for the F 1s, N 1s and P 2p photoelectrons, respectively. The small black (0°) and red (80°) numbers in the graph represent the contribution of each IL double layer to the N 1s signal, for clarity the first double layer is shaded in yellow.

From these considerations, it is evident that the surface sensitivity of ARXPS can be varied by changing the electron emission angle: Thereby, a higher peak intensity in 80° (surface-sensitive) compared to 0° (bulk-sensitive) indicates a higher concentration of this species in the topmost layer than in the bulk and vice versa.

3 Materials, Instrumentation and Experimental Details

3.1 Chemicals and Sample Preparation

An overview of the ILs investigated in the course of this thesis is given in Table 3.1 including their formula, IUPAC name, molecular structure and the respective melting temperature, T_m, or glass transition temperature, T_g.

1-Ethyl-3-methylimidazolium hexafluorophosphate, $[C_2C_1Im][PF_6]$, and 1-butyl-3-methylimidazolium hexafluorophosphate, $[C_4C_1Im][PF_6]$, were purchased from Merck (purity for synthesis) and Iolitec (purity 99.5%), respectively. 1-Butyl-3-methylimidazolium tetrafluoroborate, $[C_4C_1Im][BF_4]$, and 1-methyl-3-octylimidazolium hexafluorophosphate, $[C_8C_1Im][PF_6]$, were purchased from Sigma-Aldrich (purities 99.9% and > 95%, respectively). 1-Methyl-3-octylimidazolium bis[(trifluoromethyl)sulfonyl]imide, $[C_8C_1Im][Tf_2N]$, was prepared by Dr. Nicola Taccardi according to literature.[87] 1,3-Di(methoxy)imidazolium hexafluorophosphate, $[(MeO)_2Im][PF_6]$, was synthesized by Dr. Sabine Dommer according to previous publications.[88, 89] 1-[2-(2-Methoxy-ethoxy)-ethyl]-3-methylimidazolium bis[(trifluoromethyl)sulfonyl]imide, $[Me(EG)_2C_1Im][Tf_2N]$, was synthesized by Wei Wei as published earlier.[86] 3-Methyl-1-(3,3,4,4,4-pentafluoro-butyl)imidazolium hexafluorophosphate, $[PFBMIm][PF_6]$, was prepared by Dr. Gabriel Partl as reported in literature.[45] All ILs have been investigated as received without any further purification except for a minimum of four freeze-pump cycles for $[C_4C_1Im][BF_4]$ prior to the preparation of the suspensions with phosphorene or antimonene.

To ensure proper mixing of the ILs in the investigated mixtures, acetonitrile (Sigma-Aldrich, purity 99.8%) was used as a co-solvent. For the ARXPS measurements, the respective IL or IL mixture was placed on a molybdenum reservoir with a depth of 0.5 mm with a Pasteur pipette or a spatula and afterwards spread over the whole sample holder. In the case of IL mixtures, the sample holder was sometimes heated up to ~65 °C to accelerate the vaporization of the solvent acetonitrile. In the case of the phosphorene and antimonene samples, a clean gold foil was used as support for the suspensions. After sample preparation, the sample is introduced into the load lock system of the UHV measuring apparatus.

Table 3.1: Overview of names, molecular structures and phase transition temperatures (T_m or T_g) of the investigated ILs.

Short Name	IUPAC Name	Molecular Structure	T_m or T_g in °C[a]
[C$_2$C$_1$Im][PF$_6$]	1-ethyl-3-methylimidazolium hexafluorophosphate		$T_m \sim 60$[90, 91]
[C$_2$C$_2$Im][PF$_6$]	1,3-diethylimidazolium hexafluorophosphate		$T_m = 70$[92]
[C$_4$C$_1$Im][BF$_4$]	1-butyl-3-methylimidazolium tetrafluoroborate		$T_g \sim -84$[93, 94]
[C$_4$C$_1$Im][PF$_6$]	1-butyl-3-methylimidazolium hexafluorophosphate		$T_g \sim -77$[90, 91, 93, 94]
[C$_8$C$_1$Im][Tf$_2$N]	1-methyl-3-octylimidazolium bis[(trifluoromethyl)sulfonyl]imide		$T_g \sim -82$[90, 95]
[C$_8$C$_1$Im][PF$_6$]	1-methyl-3-octylimidazolium hexafluorophosphate		$T_g \sim -71$[90, 91]
[(MeO)$_2$Im][PF$_6$]	1,3-di(methoxy)imidazolium hexafluorophosphate		$T_m = 83 - 84$[96]
[Me(EG)$_2$C$_1$Im][Tf$_2$N]	1-[2-(2-methoxy-ethoxy)ethyl]-3-methylimidazolium bis[(trifluoromethyl)sulfonyl]imide		n/a
[PFBMIm][PF$_6$]	3-methyl-1-(3,3,4,4,4-pentafluorobutyl)imidazolium hexafluorophosphate		$T_m = 66$[45]
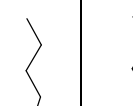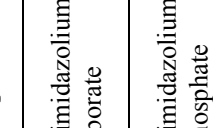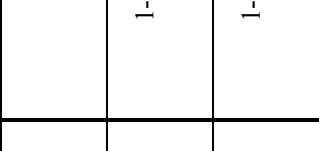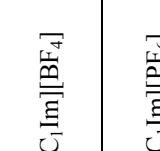
a) strongly depends on method, contamination level, etc.

3.2 Dual Analyzer System for Surface Analysis

Commonly ARXPS is performed by either tilting the sample to achieve grazing emission or by rotating the analyzer to gain the more surface-sensitive information as described in Chapter 2. In Figure 3.1, the UHV chamber, the so-called Dual Analyzer System for Surface Analysis (DASSA),[97] is sketched. This setup was developed in cooperation with Omicron NanoTechnology and was used for the acquisition of most ARXPS data presented in this thesis. It was built for investigating macroscopic amounts of liquid samples and has a base pressure below $1 \cdot 10^{-10}$ mbar. The DASSA setup consists of three separated main parts: Preparation chamber, analysis chamber and load lock system. In the following, the equipment used throughout this thesis is described in more detail. Further details are provided in Ref. [97].
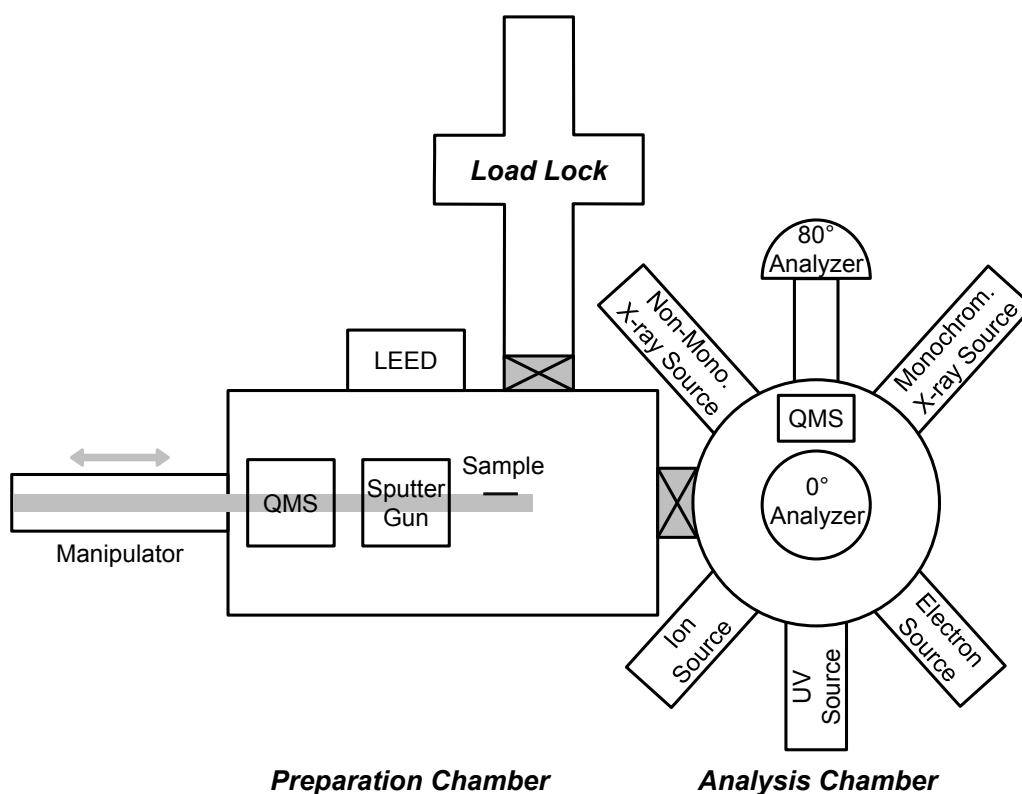
Figure 3.1: Scheme of the DASSA setup showing the three main parts: Preparation chamber (left), analysis chamber (right) and load lock system (top), as well as the components mounted to the respective chamber part.

Inside the UHV chamber, the samples typically are kept in horizontal position, so no dripping of the IL can occur. The samples are introduced into the load lock system and are degassed there for at least twelve hours. Afterwards, they are transferred onto the manipulator in the preparation chamber. The manipulator head has two sample stages

available: A low (equipped with liquid nitrogen cooling and radiative heating) and a high (with heating by electron bombardment) temperature stage. Throughout this thesis, mainly the low temperature stage with a temperature range between −123 and 1027 °C is used. For cleaning the molybdenum reservoirs of the sample holders as well as for occasional surface cleaning of the investigated samples, a sputter gun (initially: Omicron NanoTechnology ISE 5; now: SPECS IQE 11/35) for Ar^+ bombardment is mounted in the preparation chamber. Furthermore, a quadrupole mass spectrometer (QMS; HIDEN HAL 3F 511) and low energy electron diffraction (LEED; Omicron) optics are mounted at the preparation chamber.

Two identical hemispherical ARGUS electron analyzers from Omicron NanoTechnology are attached to the analysis chamber. They are mounted under an emission angle of 0° and 80° relative to the surface normal of a horizontally mounted sample holder on the manipulator. This configuration allows for simultaneous measurements of the same sample spot and therefore reduces the X-ray exposure time by about a factor of two compared to conventional ARXPS setups performing two consecutive measurements for both emission angles. The MATRIX T3.2 software was customized specifically for the DASSA setup for the simultaneous operation of both analyzers. A monochromated Al K_α X-ray source (Omicron XM 1000; $hv = 1486.6$ eV), operated at 238 W, is mounted in a magic angle configuration with respect to both analyzers. Survey scans are either recorded with 200 or 150 eV pass energy, whereas for region scans a pass energy of 35 eV is used resulting in an overall energy resolution of 0.4 eV. Moreover, a dual non-monochromated X-ray source (Omicron DAR 400) with Mg K_α ($hv = 1253.6$ eV) and Al K_α ($hv = 1486.6$ eV) radiation, an ion source (Omicron FIG 05), an electron source (Omicron CN 10), an ultraviolet source (UV source; Omicron HIS 13) and a QMS (Pfeiffer Vacuum PrismaPlus QMG 220) are mounted at the analysis chamber but have not been used in the course of this thesis.

3.3 Data Evaluation

In the following, the general procedure for the data evaluation is described. For more details, see the respective published peer-reviewed articles [P1] – [P5].

For the data evaluation, the CasaXPS (version 2.3.16Dev6) software is used for all spectra recorded at the DASSA setup. For the quantification, the atomic sensitivity factors (ASFs) are taken into account for each individual spectrum to correct *e.g.* different cross sections. A list of the ASFs used in this thesis is given in Table 3.2.[97]

Table 3.2: ASFs applied to the peak intensities for measurements carried out at the DASSA setup.

Core Level	ASF_{DASSA}
F 1s	1.00
O 1s	0.67
N 1s	0.46
C 1s	0.30
S 2p	0.64
P 2p	0.46
B 1s	0.15

Commonly, a two point linear background is subtracted from the XP spectra, only when the IL contains a CF_x group like in the $[PFBMIm]^+$ cation or the $[Tf_2N]^-$ anion a three point linear background is subtracted from the C 1s spectrum. All peaks are fitted with a Gauss-Lorentz function with 30% Lorentzian contribution. The S 2p and P 2p spectra consist of the two spin-orbit-split components $2p_{1/2}$ and $2p_{3/2}$. These two peaks are fitted with the same full width at half maximum (FWHM), a $1 : 2$ area ratio and peak separations of 1.21 and 0.90 eV in the S 2p and P 2p spectra, respectively. For fitting the C 1s region different constraints are applied: For ILs consisting of the non-functionalized $[C_nC_1Im]^+$ cation, the area of the $C_{hetero'}$ peak is four times the area of the C_2 peak (for peak assignment see Figure 3.2) and both peaks are separated by 0.9 eV. The $C_{hetero'}$ peak is 1.1 times wider than the C_2 and the C_{alkyl} peaks. For the $[(MeO)_2Im]^+$ cation, the $C_{hetero'}$ peak is 1.02 times wider and four times more intense than the C_2 peak and both peaks are separated by 1.10 eV. For the $[PFBMIm]^+$ cation, the $C_{hetero'}$ peak is 1.33 times wider than the C_2 peak and both peaks are separated by 1.02 eV. Since the C_{CF3} peak overlaps with the shake-up of the aromatic system of the imidazolium ring,[98] its intensity is set equal to the

intensity of the C_{CF2} peak for quantification. All those constraints are applied to the spectra recorded in 0° and 80° emission.
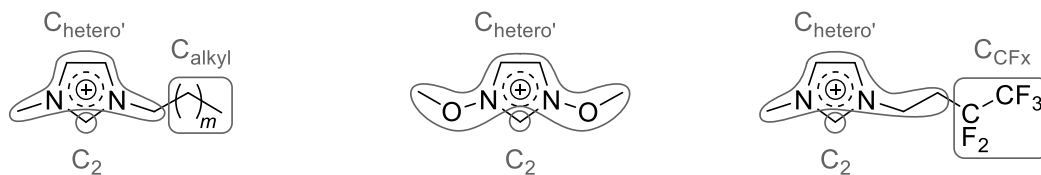
Figure 3.2: Peak assignment for the C 1s species C_2, $C_{hetero'}$, C_{alkyl} and C_{CFx} in different cations: $[C_nC_1Im]^+$, $[(MeO)_2Im]^+$ and $[PFBMIm]^+$. Adapted from [P3] and [P4] under license CC BY 4.0.

Additional constraints are applied for the mixtures published in [P4]. The F_{PF6} peak in the F 1s spectra is 0.79 times wider than the F_{CFx} peak and in the N 1s region the N_{MeO} and N_{PFB} peaks are set to equal width. Due to only a very weak N_{PFB} signal in the 95 mol% mixture of $[(MeO)_2Im][PF_6]$ and $[PFBMIm][PF_6]$, the peak separation is constrained to 1.40 ± 0.04 eV. For all mixtures in this paper, the C_2 to $C_{hetero'}$ ratio is set to the nominally expected ratio resulting from the molar ratio of the two ILs.

A lower intensity is detected for spectra recorded under an emission angle of 80° compared to 0° emission. To compensate for this, the 80° spectra are scaled up by a so-called geometry factor[97] to facilitate the visual comparison of both spectra showing enrichment and depletion effects directly.

4 Results and Discussion

Within this thesis, five peer-reviewed articles have been published and are summarized in this chapter. Some additional results, which are unpublished, are included to support the published results. For further experimental details see the respective publications [P1] – [P5].

4.1 Surface Composition and Surface Tension of Homologue Ionic Liquids[P1]

In contrast to all other data presented in this thesis, the XPS data shown in this chapter are measured in a different UHV setup equipped with a non-monochromated Al K_α X-ray source and one analyzer attached, which requires a tilting of the sample for surface-sensitive 80° emission measurements. This UHV setup was described in detail earlier.[99-103] In contrast to the data recorded at the DASSA setup, the C_2 and $C_{hetero'}$ peaks are combined in one C_{hetero} peak due to a lower energy resolution resulting from the non-monochromated X-ray source of this setup.

The aim of this study was to combine ARXPS measurements and MD simulations to determine the outer surface composition of the homologue series of $[C_nC_1Im][Tf_2N]$ with $n = 2, 4, 6, 8, 10$ and 12, and to derive the surface tension values for these six ILs applying the so-called Langmuir principle. In 1917 and 1930, Langmuir stated that the surface free energy of a liquid as deduced by surface tension measurements is the result of "the structure of the surface layer of atoms"[104] and is thus influenced by the orientation of surface molecules as well as the intermolecular interaction not only at the surface but also "of the atoms underlying the surface".[105] The ILs' molecular orientation at the surface was probed by means of ARXPS[99] whereas the density profiles were recently simulated by MD performed by Dr. Karina Shimizu.[106] The density of groups at the outer surface determined by MD simulations (in particular, the number of surface aliphatic chains and ionic head groups) were then used to calculate the surface tension values for each of the $[C_nC_1Im][Tf_2N]$ ILs according to the Langmuir principle and compared to the surface tension values experimentally determined for all six ILs under identical conditions.[86]

In the course of this thesis, a re-evaluation of the existing ARXPS data was necessary to allow for a more accurate quantitative comparison with the MD results. In previous publications,[42, 52, 86, 99] the surface enrichment of the alkyl chains relative to the cationic head groups in the $[C_nC_1Im][Tf_2N]$ series was determined by the intensity ratios of the C_{alkyl} to C_{hetero} intensities as derived solely from fitting the C 1s ARXP spectra. However, the small peak separation between C_{alkyl} and C_{hetero} of ~1.5 eV leads to rather high uncertainties of the $I(C_{alkyl})$ / $I(C_{hetero})$ values in the 80° spectra, particularly for large n values with a strongly dominating C_{alkyl} signal next to a small C_{hetero} shoulder.

To overcome this difficulty and to obtain more accurate results, the N 1s spectra with the well-separated N_{Im} signals of the nitrogen atoms of the imidazolium ring in direct proximity to the C_{hetero} atoms are additionally taken into account as internal reference.[106] The intensity change of the N_{Im} peak is used to determine the corrected 80° C_{hetero} intensity: $I_{corr}(C_{hetero,80°})$ = $[I(N_{Im,80°})$ / $I(N_{Im,0°})]$ · $I(C_{hetero,0°})$. This intensity is then subtracted from the combined C_{hetero} and C_{alkyl} signal in 80° to obtain the corrected C_{alkyl} intensity in 80° emission. This re-evaluation provides corrected $I(C_{alkyl})$ / $I(C_{hetero})$ ratios in 80° with a higher accuracy (about ±8%), and reveals that the surface enrichment of the long alkyl chains was underestimated previously.[99] In Figure 4.1a, the corrected 80° ratios (full red squares) systematically lay above the previously published ratios (open red triangles).

For the comparison with the corrected ARXPS results, density profiles of the MD simulations, performed by Dr. Karina Shimizu, are analyzed assuming an exponential decay of the contribution as expected from the ARXPS signal attenuation depicted in Figure 2.3. From these surface profiles, the ratios of the terminal methyl carbon atom of the alkyl chain (representing C_{alkyl}) and the C_2 atom (representing C_{hetero}), weighted by the respective nominal atom numbers of these atoms, $(n\text{-}1)$ / 5, are shown in Figure 4.1a as crosses (0° in black and 80° in red) to obtain the respective simulated C_{alkyl} to C_{hetero} ratio. Considering the assumptions made for the simulations, the corrected experimental and simulated ratios overall are in good agreement.

To derive the experimental surface tension values[86] from MD simulations using the Langmuir principle, the cationic head groups (represented by the C_2 atom) and the $[Tf_2N]^-$ anions (represented by the N_{Tf2N} atom) are assumed to contribute equally to the surface tension of 36.3 mN/m for $[C_1C_1Im][Tf_2N]$. Furthermore, the nearly constant

surface tension of 29.5 mN/m for $[C_nC_1Im][Tf_2N]$ with $n = 8$, 10 and 12 (blue triangles in Figure 4.1b) is assumed to be built up only by the surface alkyl chains (represented by the terminal methyl carbon atom). Then, the surface tension for each of the $[C_nC_1Im][Tf_2N]$ ILs is calculated by the sum over the contributions of the three different atoms being present at the MD simulated outer surface (note that the atoms are weighted by their respective molar volume). Comparing the values received from the simulations with the measured surface tension values, they are in good agreement assuming an outer surface layer thickness of 0.54 up to 0.93 nm for $[C_nC_1Im][Tf_2N]$ with $n = 2$ to 12, that would correspond to an emission angle of 87.5° in ARXPS (see Figure 4.1b). Note that such pronounced grazing emission conditions are impractical for our ARXPS setup due to sample holder shielding. In contrast, the employed 80° geometry probes between 0.91 and 1.31 nm for $[C_2C_1Im][Tf_2N]$ and $[C_{12}C_1Im][Tf_2N]$, respectively, which is more than just the topmost surface layer of the ILs as it is evident from Figure 2.3.
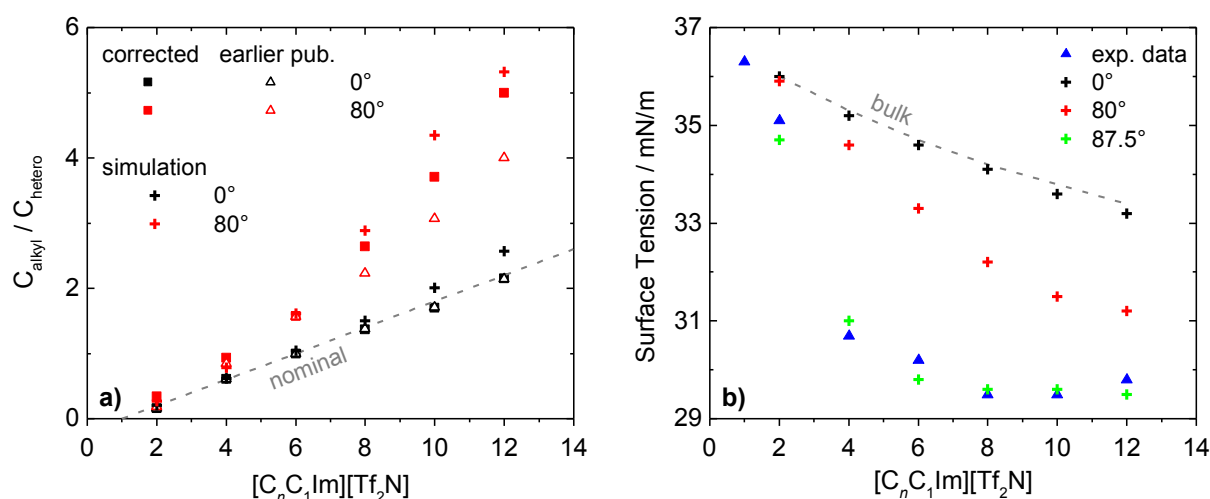
Figure 4.1: a) C_{alkyl} / C_{hetero} ratios for varying alkyl chain length, n, in the $[C_nC_1Im][Tf_2N]$ series. The corrected ARXP intensity ratios are given as full squares and the earlier published (earlier pub.) intensity ratios as open triangles for 0° (black) and 80° (red) emission, respectively. The ratios deduced from the density profile analysis (simulation) using an exponential decay are included as crosses. The nominally expected C_{alkyl} / C_{hetero} ratio is indicated by the dashed gray line. b) Surface tension values for varying alkyl chain length, n, in the $[C_nC_1Im][Tf_2N]$ series. The blue triangles refer to the experimentally obtained surface tension values (exp. data)[86] and the crosses represent the values obtained from the density profile analysis assuming ARXP emission angles of 0° (black), 80° (red) and 87.5° (green). The surface tension of the bulk composition using the Langmuir principle is given as dashed gray line. Adapted from [P1] with permission from "Langmuir".

In this investigation, the concept formulated by Langmuir about 100 years ago was most likely used in such explicit way for the first time to understand the surface tension data of highly structured fluids such as ILs. Combining ARXPS measurements and MD

simulations, the composition of the outer surface could be determined consistently, and a correct estimation of the complex surface tension trend within the $[C_nC_1Im][Tf_2N]$ series could be derived applying the Langmuir principle of surface group contributions in a quantitative way.

4.2 Binary Mixtures Containing Functionalized Ionic Liquids

Over the last two decades, many surface science studies have been carried out revealing information about the surface composition and electronic structure of neat ILs containing a wide variety of cations and anions.[8, 42-53, 61-64, 67-72, 87, 99, 107-122] To extend this understanding, IL mixtures got more into the focus of research recently. Up to now, mainly mixtures of two non-functionalized imidazolium-based ILs[8, 9, 44, 50-52, 54-56, 58-61, 63-67] have been investigated and only few examples are found in literature discussing mixtures containing functionalized imidazolium-based cations.[45, 60, 70]

The aim of this chapter is to extend the knowledge about the surface composition of interesting methoxy-functionalized ($[(MeO)_2Im][PF_6]$) and fluorinated ($[PFBMIm][PF_6]$) ILs. Oxygen atoms, like in the methoxy groups of $[(MeO)_2Im][PF_6]$, are additional hydrogen bond acceptor sites in the ILs resulting in promising properties *e.g.* for the extraction of estrogens or analgesics from aqueous solutions and the dissolution of greenhouse gases like N_2O and CO_2.[27, 88, 123-126] Furthermore, the oxygen functionalization can decrease the toxicity as well as increase the biodegradability of the ILs.[127, 128] Fluorinated chains such as in $[PFBMIm][PF_6]$ tend to agglomerate forming fluorous domains in addition to the well-known polar and non-polar domains in non-fluorinated ILs.[3, 70, 71, 129] Generally, properties and domain structures of ILs can be tuned by changing the chain length in neat ILs and the composition in IL mixtures.[4, 60, 70] Commonly, the surface tension of fluorinated ILs is lower compared to their alkylated analogues[60, 130, 131] and they are potential candidates to replace harmful fluorine-containing solvents like lubricants, coolants in refrigerators and others.[4, 129]

In this chapter, the knowledge about the surface enrichment and depletion effects is extended to binary IL mixtures containing both non-functionalized and functionalized cations as well as mixtures with methoxy-functionalized and fluorinated imidazolium-based cations. In addition, the effect of temperature on the surface enrichment and depletion is studied.

4.2.1 Equimolar Mixtures of Methoxy- and Non-Functionalized Ionic Liquids[P2]

Surface enrichment and depletion effects have been investigated in equimolar binary mixtures of a methoxy-functionalized IL, $[(MeO)_2Im][PF_6]$, and two non-functionalized ILs, $[C_8C_1Im][PF_6]$ and $[C_8C_1Im][Tf_2N]$. The neat ILs as well as the mixtures are all studied at 90 °C to ensure measurements in their liquid state. Both mixtures either consist of ILs with a common $[PF_6]^-$ anion and two different cations, or are composed of four different ions.

Due to unique core level signals and chemical shifts of the various ions in ARXPS, it is possible to distinguish between both cations, $[(MeO)_2Im]^+$ and $[C_8C_1Im]^+$, as well as between the two anions, $[PF_6]^-$ and $[Tf_2N]^-$. In $[(MeO)_2Im][PF_6]$, the two oxygen atoms, O_{MeO}, directly bound to the nitrogen atoms of the imidazolium ring influence the electronic structure of the cation strongly, resulting in a binding energy of 403.6 eV for the N_{MeO} signal of the cation. In contrast, the N_{Im} signal of the $[C_8C_1Im]^+$ cation is located at 402.2 eV, corresponding to a shift of ~1.4 eV (see Figure 4.2–I, II and III). Furthermore, the carbon atoms of the imidazolium ring of the $[(MeO)_2Im]^+$ cation are shifted to higher binding energy by 0.2 to 0.4 eV, compared to the C_2 and $C_{hetero'}$ peaks of $[C_8C_1Im]^+$. The O_{MeO} signal is located at 535.3 eV, that is, ~2.7 eV higher compared to the O_{Tf2N} peak of $[C_8C_1Im][Tf_2N]$ at 532.6 eV (see Figure 4.2–I and II).

These strong chemical shifts of the $[(MeO)_2Im]^+$ cation are remarkable and will be discussed first. In literature, only very few examples of such high oxygen binding energies are reported, e.g. in peroxo-oxygen-functionalized polymers.[132] Typically, oxygen atoms located in the chains of IL cations, like in the polyethylene glycol-functionalized IL $[Me(EG)_2C_1Im][Tf_2N]$, exhibit binding energies of ~532.7 eV which is very similar to the binding energy position of the oxygen atoms in the $[Tf_2N]^-$ anions.[96, 99] Moreover, the N 1s binding energy of the nitrogen atoms of the imidazolium ring of this IL and $[C_8C_1Im][Tf_2N]$ is about the same, excluding a pronounced impact of the oxygen functionality on the electronic structure of the $[Me(EG)_2C_1Im]^+$ head group. Very recently, other ether-functionalized ILs have been investigated by XPS revealing negligible binding energy shifts in the N 1s region and, compared to $[(MeO)_2Im][PF_6]$, only small O 1s peak shifts.[68]
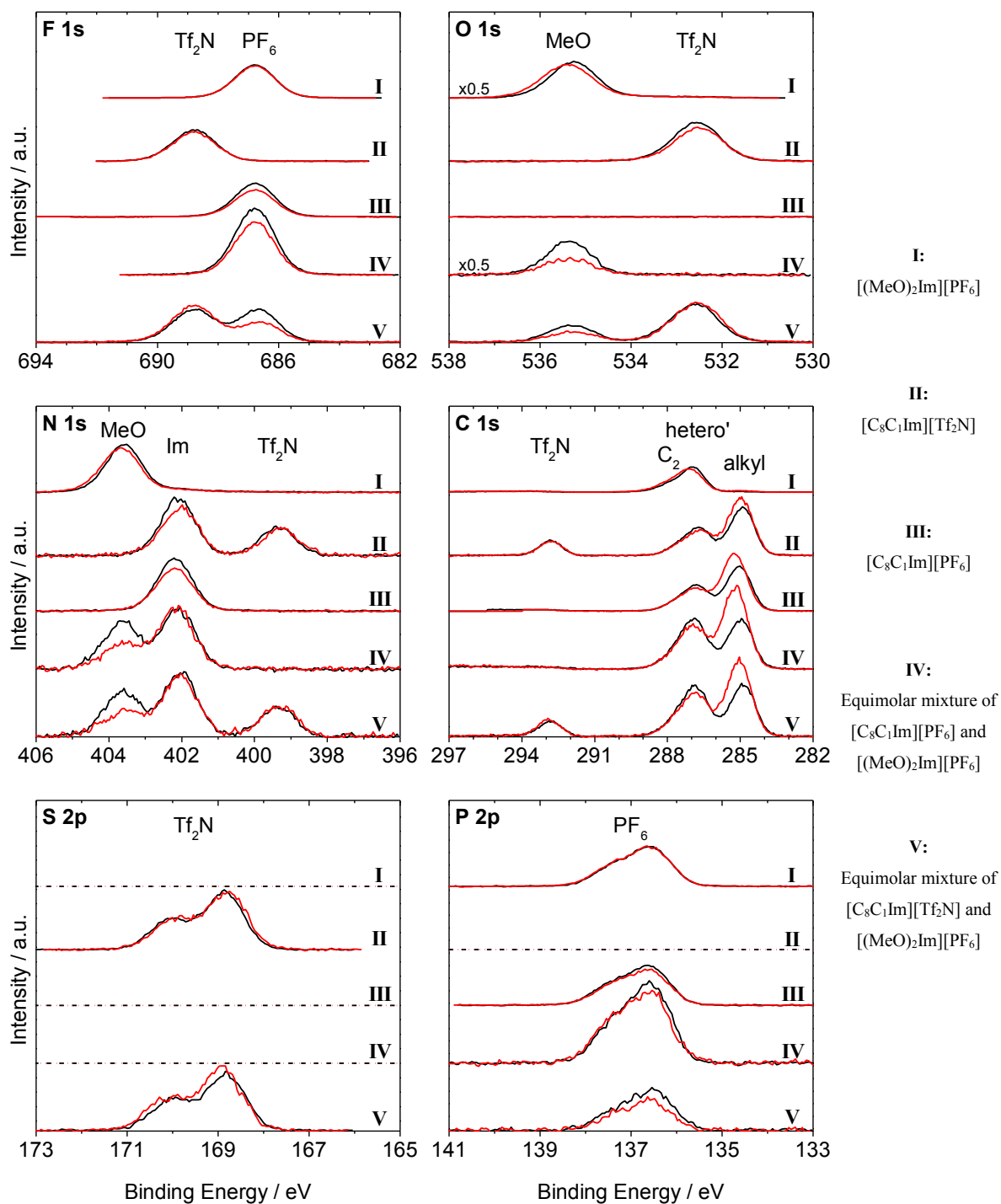
Figure 4.2: ARXP spectra of the neat ILs $[(MeO)_2Im][PF_6]$ (I), $[C_8C_1Im][Tf_2N]$ (II) and $[C_8C_1Im][PF_6]$ (III), and the equimolar mixture of $[C_8C_1Im][PF_6]$ and $[(MeO)_2Im][PF_6]$ (IV) and the equimolar mixture of $[C_8C_1Im][Tf_2N]$ and $[(MeO)_2Im][PF_6]$ (V) recorded under 0° (black) and 80° (red) emission. The sample temperature was 90 °C. Adapted in part from [P2] under license CC BY-NC 4.0.

These particularly large chemical shifts of the XP signals of $[(MeO)_2Im][PF_6]$ are due to the extraordinary electronic structure of this cation. Density Functional Theory (DFT) calculations combined with charge distribution analysis using the natural bond orbital (NBO) methodology, performed in a collaboration by Prof. Dr. Patricia Hunt, showed that the positive charge in the cationic head group is distributed over the imidazolium ring and the adjacent oxygen atoms, O_{MeO}, resulting in an extended aromatic system (see Figure 4.3a). In contrast to the non-functionalized analogue cation, $[C_2C_2Im]^+$, the whole imidazolium ring of the $[(MeO)_2Im]^+$ cation (see Figure 4.3b) has a more positive charge of +0.93 e (vs. +0.31 e for $[C_2C_2Im]^+$; see Figure 4.3c). As a consequence, the charge on the nitrogen atoms, N_{MeO}, of the $[(MeO)_2Im]^+$ cation shows a more positive value of –0.02 e compared to –0.35 e for the N_{Im} atoms of the $[C_2C_2Im]^+$ cation.
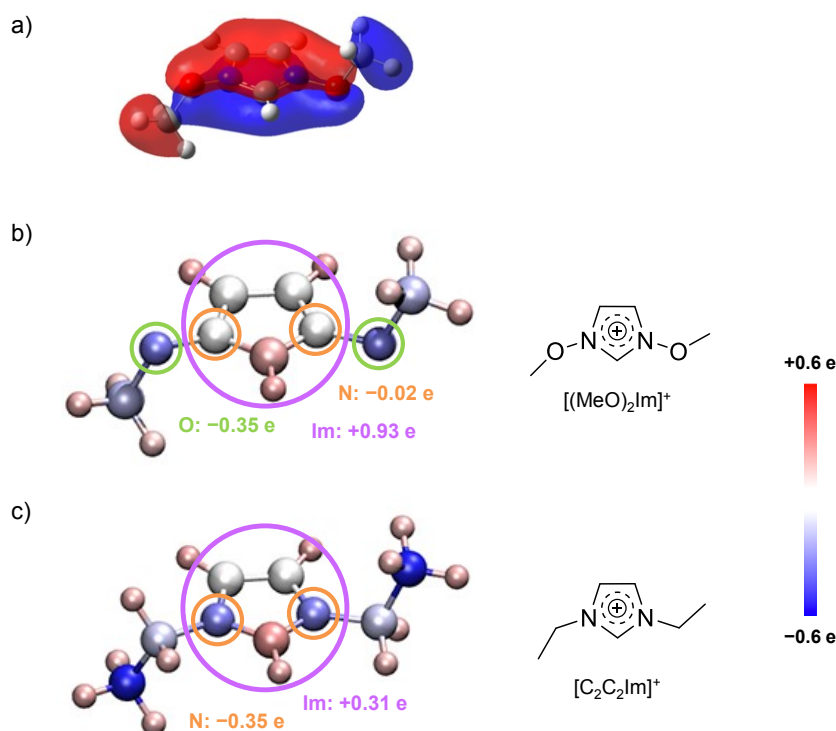
Figure 4.3: a) Molecular orbital of $[(MeO)_2Im]^+$ showing the aromatic delocalization of the positive charge over the imidazolium ring and the O_{MeO} atoms. The NBO charge distribution at the atoms of the b) $[(MeO)_2Im]^+$ cation and c) $[C_2C_2Im]^+$ cation. Red is positive and blue is negative. The charges localized in the imidazolium ring (purple) and on the nitrogen (orange) and oxygen (green) atoms are given. Adapted from [P2] under license CC BY-NC 4.0.

Next, the composition of the first 7 to 9 nm, as probed by the 0° XPS measurement, of the equimolar mixture of $[C_8C_1Im][PF_6]$ and $[(MeO)_2Im][PF_6]$ will be discussed, *i.e.* the mixture with two different cations but the common $[PF_6]^-$ anion. The cationic head groups of the ILs can be easily distinguished due to the well-separated N_{MeO} and N_{Im} peaks in the

N 1s region (see black spectrum in Figure 4.2–IV). Instead of the 1 : 1 ratio of the two nitrogen species expected for the equimolar bulk composition, the N 1s spectrum exhibits a N_{Im} to N_{MeO} ratio of 1 : 0.85 in 0° emission. This means that within the 0° XPS probing depth, a pronounced depletion of the $[(MeO)_2Im]^+$ cation from the topmost layers is found leaving the surface region enriched by the $[C_8C_1Im]^+$ cation.

The depletion of the $[(MeO)_2Im]^+$ cation from the near-surface region is also found for the equimolar mixture of $[C_8C_1Im][Tf_2N]$ and $[(MeO)_2Im][PF_6]$, *i.e.* the mixture with two different cations and two different anions. The intensities of the N_{Im} and N_{MeO} peaks in 0° (black) emission (see Figure 4.2–V) reveals a 1 : 0.77 ratio instead of the expected 1 : 1 ratio. This indicates an even more pronounced depletion of the $[(MeO)_2Im]^+$ cation from the near-surface region in comparison to the previously discussed mixture with the common $[PF_6]^-$ anion. This difference is possibly related to the slight surface enrichment of the $[Tf_2N]^-$ anion in the second mixture. In the F 1s region with the two peaks corresponding to the six fluorine atoms of the $[Tf_2N]^-$ anion at 688.8 eV and of the $[PF_6]^-$ anion at 686.7 eV (see Figure 4.2–V) the F_{Tf2N} signal is ~14% larger than the F_{PF6} peak instead of the expected 1 : 1 ratio.

The overall surface enrichment and depletion effects within the first 7 to 9 nm probed in 0° emission are much more pronounced when focusing on the outermost 1 to 1.5 nm investigated under 80° emission. In the following, surface enrichment and depletion effects of the neat ILs are briefly pointed out. Figure 4.2–I shows the ARXP spectra of $[(MeO)_2Im][PF_6]$ in 0° (black) and 80° (red) emission, revealing no changes in intensity ruling out strong preferential orientation in the surface layer. In contrast, the octyl chains of neat $[C_8C_1Im][Tf_2N]$ and $[C_8C_1Im][PF_6]$ are surface-enriched as indicated by a higher C_{alkyl} intensity in 80° compared to 0° (see Figure 4.2–II and III). The $[Tf_2N]^-$ anion signals of $[C_8C_1Im][Tf_2N]$ show a minor enrichment of the CF_3 groups along with a slight depletion of the SO_2 groups detected in the O 1s spectrum due to the lower kinetic energy (as compared to the S 2p signal). In the F 1s and P 2p spectra, a depletion of the $[PF_6]^-$ anion is observed for $[C_8C_1Im][PF_6]$ (see Figure 4.2–III).

For both IL mixtures, the surface enrichment of the $[C_8C_1Im]^+$ cation at the expense of the $[(MeO)_2Im]^+$ cation is more obvious in the 80° spectra (red in Figure 4.2–IV and V) compared to 0°. The N_{MeO} signal is lower at 80° emission whereas the N_{Im} signal has almost identical signal intensities under both emission angles. The O_{MeO} peak in the O 1s

spectra decreases roughly by the same amount as the N_{MeO} signal validating the accuracy of the measurement as these two atoms are directly bound to each other. This is in line with the observations that the $[C_8C_1Im]^+$ cation is surface-enriched at the IL/vacuum interface with its octyl chain pointing towards the vacuum as the C_{alkyl} signal gains intensity when going from 0° to 80° emission. Most likely, the driving force for the surface enrichment of the $[C_8C_1Im]^+$ cation and the depletion of the $[(MeO)_2Im]^+$ cation is to obtain an overall low surface tension. Unfortunately, the surface tension value for $[(MeO)_2Im][PF_6]$ is not known but the surface tension for ILs with the same anion but different alkyl chain lengths are available in literature.[71, 86, 111, 133-135] In general, the IL containing the longer alkyl chain, in this case $[C_8C_1Im][X]$, possesses a lower surface tension compared to that with a short chain. Moreover, oxygen atoms in the side chain might increase the surface tension in addition.[86]

For the $[Tf_2N]^-$ and $[PF_6]^-$ anions in the equimolar mixture of $[C_8C_1Im][Tf_2N]$ and $[(MeO)_2Im][PF_6]$, the enrichment and depletion in the first 1 to 1.5 nm is directly visible in the F 1s spectrum recorded at 80° (see Figure 4.2–V). The F_{Tf2N} peak is about two times higher than the F_{PF6} peak. This pronounced surface enrichment of the $[Tf_2N]^-$ anion on expense of the $[PF_6]^-$ anion goes along with the surface tension values of ILs consisting of the respective anion and a common cation. The surface tension of $[C_8C_1Im][PF_6]$ is 32.5 mN/m whereas $[C_8C_1Im][Tf_2N]$ has a lower surface tension of 29.5 mN/m which supports the observed enrichment of the $[Tf_2N]^-$ anion.[86]

4.2.2 Mixtures of Fluorinated and Non-Fluorinated Ionic Liquids[P3]

Mixtures of $[PFBMIm][PF_6]$ and $[C_4C_1Im][PF_6]$ have been investigated with different molar content of $[PFBMIm][PF_6]$ by means of temperature-dependent ARXPS from 95 °C to their onset of solidification. Both ILs consist of the same $[PF_6]^-$ anion whereas the cation differs in the functionalization of the butyl chain. In contrast to the fully hydrogenated chain in the $[C_4C_1Im]^+$ cation, the two terminal carbon atoms in the chain of the $[PFBMIm]^+$ cation are fully fluorinated, resulting in a pentafluorobutyl (PFB) chain. Due to the differences in the chemical environment of the fluorine atoms in the $[PF_6]^-$ anion compared to the ones in the $[PFBMIm]^+$ cation, two distinct peaks are detected in the F 1s region. Also the carbon atoms in both butyl chains are in different chemical environments leading to chemical shifts in the C 1s spectrum.

Starting with the neat ILs at 95 °C, the C_{alkyl} peak in the C 1s spectrum of [C_4C_1Im][PF_6] (at ~285.1 eV) is more intense in 80° (red) emission compared to 0° (black) (see Figure 4.4a–right panel), showing a slight surface enrichment of the butyl chain, as it is known from literature[53, 99] for [C_nC_1Im]$^+$ cations with an alkyl chain with $n \geq 4$. In contrast, all the other IL signals are lower in intensity in 80° with respect to the 0° measurement as depicted for the F 1s (left panel) and N 1s (middle panel) spectra in Figure 4.4a.

The ARXP spectra of [$PFBMIm$][PF_6] in Figure 4.4f show an increase of the 80° intensity of the F_{CFx} ($CF_x = CF_2 + CF_3$) peak at 688.9 eV in the F 1s spectrum and an increase of the C_{CF3} and C_{CF2} peaks at 293.6 and 291.3 eV, respectively, in the C 1s spectrum. The F_{PF6} and P_{PF6} signals of the anion at 686.8 and 137.0 eV, respectively, as well as the N_{PFB}, C_2 and $C_{hetero'}$ signals of the cationic head group at 402.2, 287.8 and 286.8 eV, respectively, are damped by the surface-enriched fluorinated chain.

Mixing [$PFBMIm$][PF_6] and [C_4C_1Im][PF_6] in molar ratios of 10, 25, 50 and 75 mol% [$PFBMIm$][PF_6] shows the same binding energy positions (within the margin of error) like in the neat ILs. Compared to neat [$PFBMIm$][PF_6], a more pronounced surface enrichment of the fluorinated chain is observed in the ARXP spectra (see Figure 4.4b – e). In Figure 4.5, this is better visualized showing the normalized ratio of the F_{CFx} and F_{PF6} content with respect to the molar ratio of the two ILs. For the 80° measurements, a higher ($F_{CFx}/F_{CFx,nom}$) / ($F_{PF6}/F_{PF6,nom}$) ratio is detected, the lower the amount of [$PFBMIm$][PF_6] in the mixture. This indicates a more pronounced surface enrichment of the fluorinated chain (compared to the nominal bulk composition) with decreasing [$PFBMIm$][PF_6] content. This enrichment is so pronounced that it is also detected in 0° emission for mixtures with 10 and 25 mol% [$PFBMIm$][PF_6]. A non-stoichiometric IL distribution in the near-surface region was recently also found for other IL systems by our group and others.[54, 96, 136] In contrast to the surface-enriched fluorinated chain, the alkyl chain of the [C_4C_1Im]$^+$ cation shows no surface enrichment in the mixtures (see Figure 4.4b – e–right panel). This is attributed to a competing effect of the fluorinated and non-fluorinated chain most likely driven by the difference in surface tension of both ILs since it is known that non-functionalized ILs usually possess a higher surface tension compared to their fluorinated analogues.[60, 130, 131]
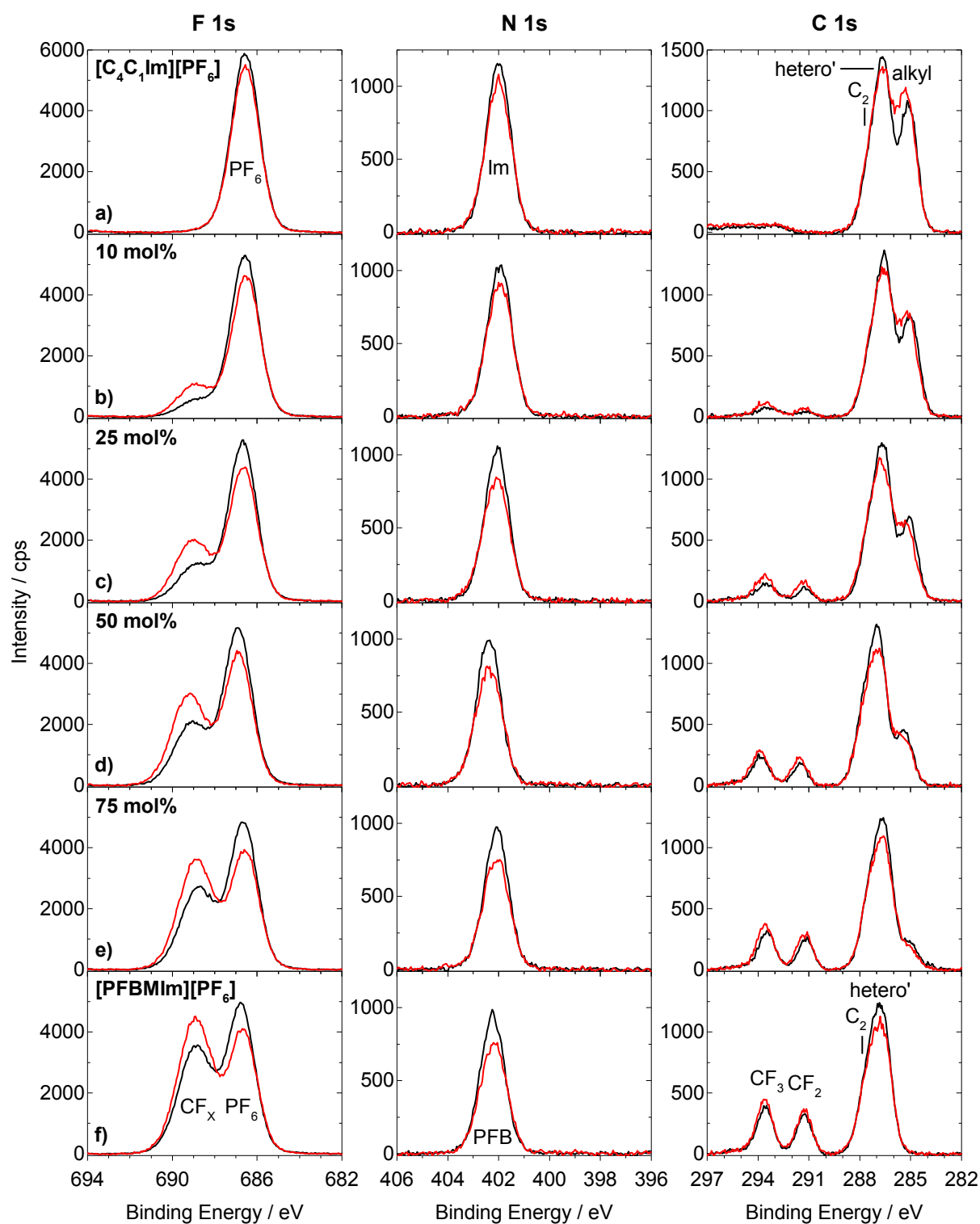
Figure 4.4: ARXP spectra recorded at 0° (black) and 80° (red) emission of a) neat $[C_4C_1Im][PF_6]$, b) – e) mixtures of $[PFBMIm][PF_6]$ and $[C_4C_1Im][PF_6]$ at molar ratios of b) 10 mol% $[PFBMIm][PF_6]$, c) 25 mol% $[PFBMIm][PF_6]$, d) 50 mol% $[PFBMIm][PF_6]$ and e) 75 mol% $[PFBMIm][PF_6]$, and f) neat $[PFBMIm][PF_6]$: F 1s (left), N 1s (middle) and C 1s (right). The sample temperature was 95 °C. Reproduced from [P3] under license CC BY 4.0.
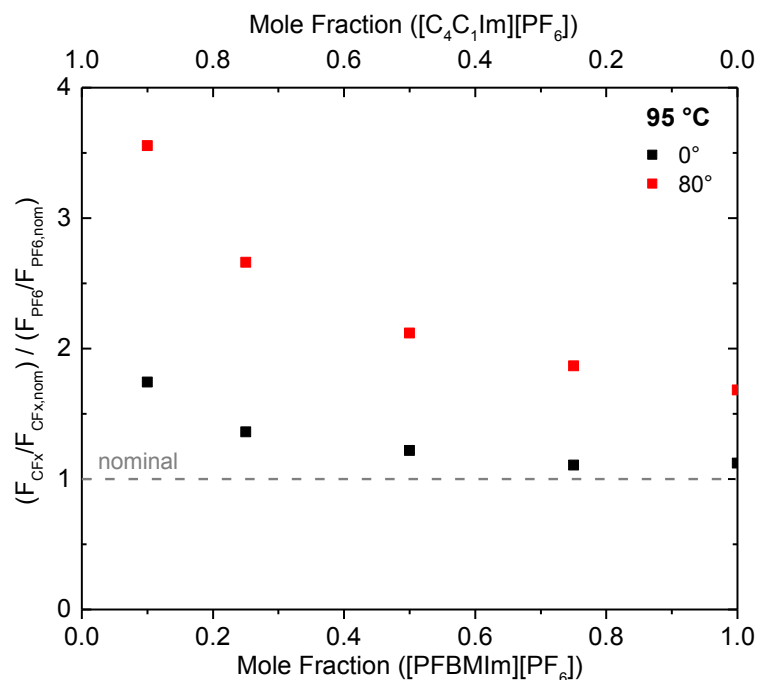
Figure 4.5: Normalized ratio of F_{CFx} and F_{PF6} at 0° (black) and 80° (red) emission. The gray dashed line indicates the nominal composition. The sample temperature was 95 °C. Adapted from [P3] under license CC BY 4.0.

In the following, temperature-dependent measurements are analyzed focusing on the 80° emission spectra, due to the higher surface sensitivity under this emission angle. By decreasing the temperature starting at 95 °C, an increase of the C_{alkyl} signal in the C 1s spectrum of neat $[C_4C_1Im][PF_6]$ is detected until −55 °C, indicating a more pronounced surface enrichment of the butyl chain. Concomitantly, the cationic head group and the $[PF_6]^-$ anion are more surface-depleted, as indicated by the decrease of intensity of the C_2, C_{hetero}, and F_{PF6} peaks. In literature,[43] such intensity changes with decreasing temperature are assigned to an increase in preferential orientation of the IL ions at the outer surface. This is attributed to an increase in entropy with a more random distribution of the alkyl chains at higher temperature.

When cooling neat $[PFBMIm][PF_6]$ from 95 to 25 °C, a moderate decrease of the F_{PF6} signal is detected in 80° without significant changes of the F_{CFx} peak intensity in the F 1s region. This shows a small increase of the surface enrichment of the fluorinated chain at the IL/vacuum interface compared to the surface depletion of the $[PF_6]^-$ anion. In Figure 4.6f, this enrichment is depicted as an increase of the normalized ratio of F_{CFx} and F_{PF6} when lowering the temperature. At 20 °C, peak broadening due to solidification of $[PFBMIm][PF_6]$ is detected.
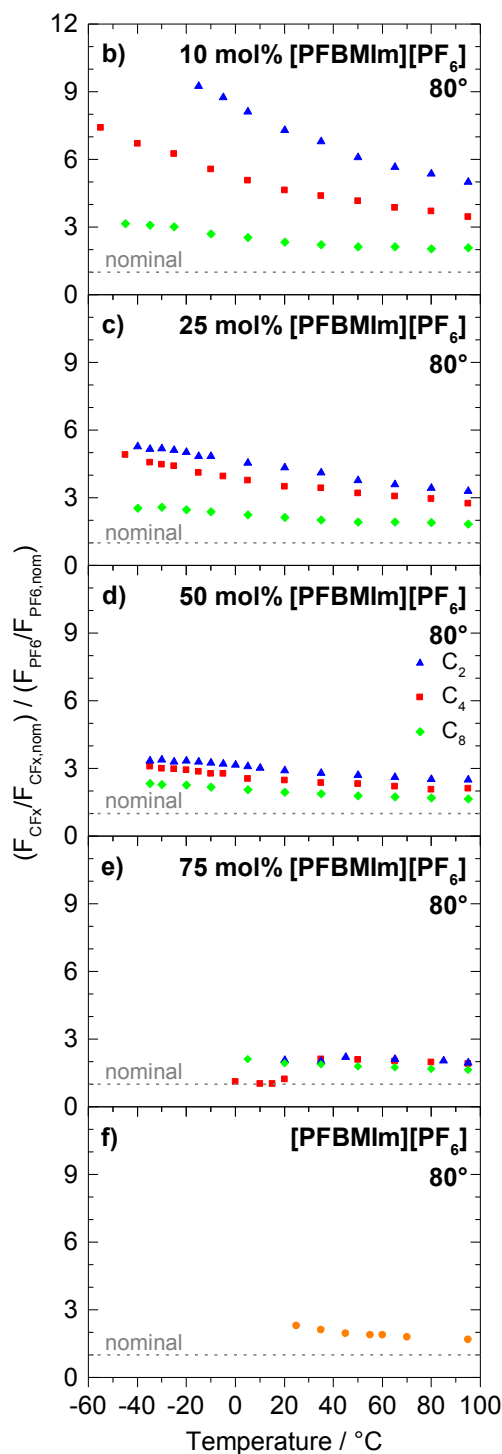
Figure 4.6: Normalized ratio of F_{CFx} and F_{PF6} at 80° emission. The measurements were started at a sample temperature of 95 °C and subsequently cooled. a) Neat $[C_nC_1Im][PF_6]$: Not shown due to the lack of a F_{CFx} signal of a fluorinated chain in the ILs, b) – e) mixtures of $[PFBMIm][PF_6]$ with $[C_nC_1Im][PF_6]$ (n = 2–blue triangles, 4–red squares, 8–green diamonds) at molar ratios of b) 10 mol% $[PFBMIm][PF_6]$, c) 25 mol% $[PFBMIm][PF_6]$, d) 50 mol% $[PFBMIm][PF_6]$ and e) 75 mol% $[PFBMIm][PF_6]$, and f) neat $[PFBMIm][PF_6]$. The gray dashed lines indicate the nominal compositions. Adapted in part from [P3] under license CC BY 4.0.

As a next step, the 10, 25 and 50 mol% mixtures of [PFBMIm][PF$_6$] and [C$_4$C$_1$Im][PF$_6$] are cooled from 95 °C until their onset of solidification, indicated by peak broadening and/or peak shifts. Depending on the composition, differences in the temperature of solidification of the supercooled mixtures are observed, *i.e.* the lower the [PFBMIm][PF$_6$] content, the lower is the onset of solidification. In general, during cooling the F$_{CFx}$ peak gains intensity which leads to an increase of the normalized ratio of F$_{CFx}$ and F$_{PF6}$ as shown in Figure 4.6b – d (red squares) at 80° emission. The observed behavior is again attributed to an increase in order at low temperature. In accordance with the F$_{CFx}$ signal, the surface enrichment of the fluorinated chain at the IL/vacuum interface is also observed in the C 1s region by an increase of the C$_{CF3}$ and C$_{CF2}$ intensities.

Cooling the 75 mol% [PFBMIm][PF$_6$] mixture from 95 to 35 °C shows the same surface enrichment behavior of the fluorinated chain of the [PFBMIm]$^+$ cation as observed for the other three mixtures previously discussed. When cooling further to 20 °C, a drastic drop of the normalized ratio of F$_{CFx}$ and F$_{PF6}$ is detected (red squares in Figure 4.6e), resulting from a decrease of the F$_{CFx}$ intensity by ~40% whereas the F$_{PF6}$ intensity stays constant. In the C 1s spectrum, a simultaneous decrease of the C$_{CF3}$ and C$_{CF2}$ signals is observed while the C$_{alkyl}$ signal of the [C$_4$C$_1$Im]$^+$ cation gains intensity. Upon further cooling, no additional changes are observed in the XP spectra until at around −10 °C peak broadening due to solidification starts. The sudden intensity decrease of the signals of the fluorinated chain of the [PFBMIm]$^+$ cation is attributed to a partial depletion of this cation from the XPS detection volume, resulting in a [C$_4$C$_1$Im]$^+$-rich mixture at the IL/vacuum interface. This is indicated by the increase of the signal of the butyl chain.

Indeed, the differential scanning calorimetry (DSC) measurement of the 75 mol% mixture (performed by Dr. Mikhail Gantman) in Figure 4.7 shows an exothermal peak at around 18 °C when cooling (blue) the sample which is attributed to the solidification of parts of the mixture. Subsequently, heating the 75 mol% [PFBMIm][PF$_6$] mixture up to 95 °C shows the same ARXP spectra (within the margin of error) as before starting the cooling series. This indicates the reversibility of the experiment.
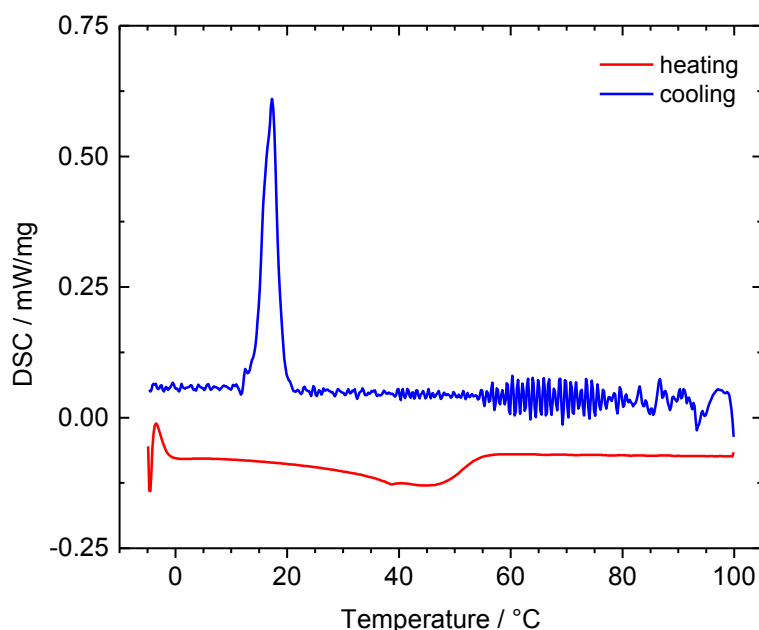
Figure 4.7: DSC measurement of a 75 mol% mixture of [PFBMIm][PF$_6$] and [C$_4$C$_1$Im][PF$_6$] showing the solidification of at least parts of this mixture around 18 °C. The heating and cooling rates were 2 K/min.

In the course of this experimental series, additional experiments with mixtures of [PFBMIm][PF$_6$] and [C$_2$C$_1$Im][PF$_6$] or [C$_8$C$_1$Im][PF$_6$], respectively, have been performed to check the influence of different alkyl chain lengths, n, on the surface enrichment of the fluorinated chain in the [PFBMIm]$^+$ cation. In the following, only the temperature-dependent measurements are discussed and are included in Figure 4.6b – e as blue triangles for the mixtures of [PFBMIm][PF$_6$] and [C$_2$C$_1$Im][PF$_6$] and as green diamonds for the mixtures of [PFBMIm][PF$_6$] and [C$_8$C$_1$Im][PF$_6$], for more details see Chapter 9.2.3.

In Figure 4.6b – e, the normalized ratios of F$_{CFx}$ and F$_{PF6}$ of the mixtures of [PFBMIm][PF$_6$] with [C$_n$C$_1$Im][PF$_6$] with $n = 2$, 4 and 8 are shown. When decreasing the temperature, an overall increase of the ratios is observed for all mixtures. Taking a closer look at the values of the ratio for the 10, 25, 50 and 75 mol% mixtures including different chain lengths, two trends are noticed: The lower the amount of [PFBMIm][PF$_6$] in the mixture, the more pronounced is the surface enrichment of the fluorinated chain compared to the [PF$_6$]$^-$ anion in the bulk. The second trend is that the shorter the alkyl chain, the higher is the normalized ratio of F$_{CFx}$ and F$_{PF6}$, *i.e.* the mixtures containing [C$_2$C$_1$Im][PF$_6$] give the highest ratios whereas the mixtures with [C$_8$C$_1$Im][PF$_6$] show the lowest ratios. This difference is attributed to a competing effect of the alkyl chain of the [C$_n$C$_1$Im][PF$_6$] with the fluorinated chain of the [PFBMIm][PF$_6$]. Luís *et al.*[71] showed that in 1-alkyl-3-methylimidazolium perfluorobutanesulfonate, [C$_n$C$_1$Im][C$_4$F$_9$SO$_3$] (with $n = 2$, 4, 6, 8, 10

and 12), which contains fluorinated chains and alkyl chains, the fluorinated chain dominates the IL/vacuum interface for $n \leq 4$. Reaching $n = 4$, the alkyl chains also start pointing towards the surface. When further increasing the chain length, this competition becomes more pronounced with the alkyl chains dominating the surface. This is in line with the findings mentioned above that the most pronounced surface enrichment of the fluorinated chain is detected for the mixtures of [PFBMIm][PF$_6$] and [C$_2$C$_1$Im][PF$_6$] compared to the mixtures of [PFBMIm][PF$_6$] with [C$_4$C$_1$Im][PF$_6$] or [C$_8$C$_1$Im][PF$_6$].

At the end of this chapter, it should be noted that another fluorinated IL was investigated in the course of these ARXPS binary mixture studies, namely the protic IL 3-methyl-2-((3,3,4,4,4-pentafluorobutyl)thio)imidazolium bis[(trifluoromethyl)sulfonyl]-imide, [C$_1$S(PFB)HIm][Tf$_2$N]. Due to decomposition during heating and X-ray exposure, this IL was not suitable for further investigations neither as neat IL nor in mixtures with [C$_4$C$_1$Im][PF$_6$]. For details see Chapter 9.2.1.

4.2.3 Mixtures of Methoxy-Functionalized and Fluorinated Ionic Liquids[P4]

The two previous chapters discussed mixtures of two differently functionalized ILs with non-functionalized [C$_n$C$_1$Im][X] ILs. In the following, mixtures containing both functionalized imidazolium-based ILs, [(MeO)$_2$Im][PF$_6$] and [PFBMIm][PF$_6$], will be presented.

Temperature-dependent measurements from 95 °C to lower temperature of three mixtures of [(MeO)$_2$Im][PF$_6$] and [PFBMIm][PF$_6$] with molar ratios of 50, 90 and 95 mol% [(MeO)$_2$Im][PF$_6$] have been performed. Both ILs consist of the same [PF$_6$]$^-$ anion but differ in the functionalization of their cation either containing oxygen or fluorine atoms. In the ARXP spectra, a differentiation of the two cations is possible due to differences in the electronic structure of both head groups resulting in the aforementioned chemical shift in the N 1s spectra (see Chapter 4.2.1). Therefore, orientation, enrichment and depletion effects are possible to identify.

The ARXP spectra of [PFBMIm][PF$_6$] as well as spectral changes by decreasing the temperature until solidification have already been discussed in Chapter 4.2.2 in detail. Briefly, the fluorinated chain is surface-enriched with respect to the [PF$_6$]$^-$ anion which is

even more pronounced when lowering the temperature as can be seen by an increase in the F_{CFx}, C_{CF3} and C_{CF2} intensities in Figure 4.8a.

For [(MeO)$_2$Im][PF$_6$], no preferential orientation is detected at 95 °C[136] in Figure 4.8e and the spectra are almost identical to the ones presented in Chapter 4.2.1 recorded at 90 °C.[96] When cooling [(MeO)$_2$Im][PF$_6$] from 95 to 50 °C, no changes occur in the ARXP spectra except for an additional peak arising around 401.5 eV in the N 1s spectrum, which is attributed to beam damage due to a prolonged radiation time. Furthermore, the beam damage is also seen by a shift of about –0.3 eV of all core levels when comparing the spectra recorded at 95 and 50 °C. Heating the sample back to 95 °C gives the original peak positions (within the margin of error) and the shoulder in the N 1s region decreases significantly. Note that no beam damage effects are detected for any of the mixtures discussed below.

Gaining knowledge about the surface enrichment and depletion of the two distinct cations in the mixtures of [(MeO)$_2$Im][PF$_6$] and [PFBMIm][PF$_6$] was the main goal when investigating the mixtures with 50, 90 and 95 mol% [(MeO)$_2$Im][PF$_6$]. At 95 °C, the surface enrichment of the fluorinated chain of the [PFBMIm]$^+$ cation is deduced from the increase in F_{CFx}, C_{CF3} and C_{CF2} intensity when going from 0° (black) to 80° (red) emission (see Figure 4.8b – d). In contrast, the F_{PF6} and P_{PF6} signals are lower in intensity in 80° compared to 0° revealing the surface depletion of the [PF$_6$]$^-$ anion with respect to the other moieties of the cations. Due to two well-separated peaks in the N 1s region, it is possible to distinguish between the head groups of the [PFBMIm]$^+$ and the [(MeO)$_2$Im]$^+$ cations which are located at ~402.2 and 403.3 eV, respectively. Comparing the spectra recorded under 0° and 80° emission, a surface enrichment of the head group of the [PFBMIm]$^+$ cation is deduced while the [(MeO)$_2$Im]$^+$ cation is surface-depleted, resulting from a decrease of the 80° intensity of the N_{MeO} peak and a constant or even higher N_{PFB} signal. Combining the information of the F 1s, N 1s and C 1s spectra, an enrichment of the [PFBMIm]$^+$ cation is observed in the 50, 90 and 95 mol% [(MeO)$_2$Im][PF$_6$] mixtures with the fluorinated chain pointing towards the vacuum whereas the [(MeO)$_2$Im]$^+$ cation and the [PF$_6$]$^-$ anion are surface-depleted.
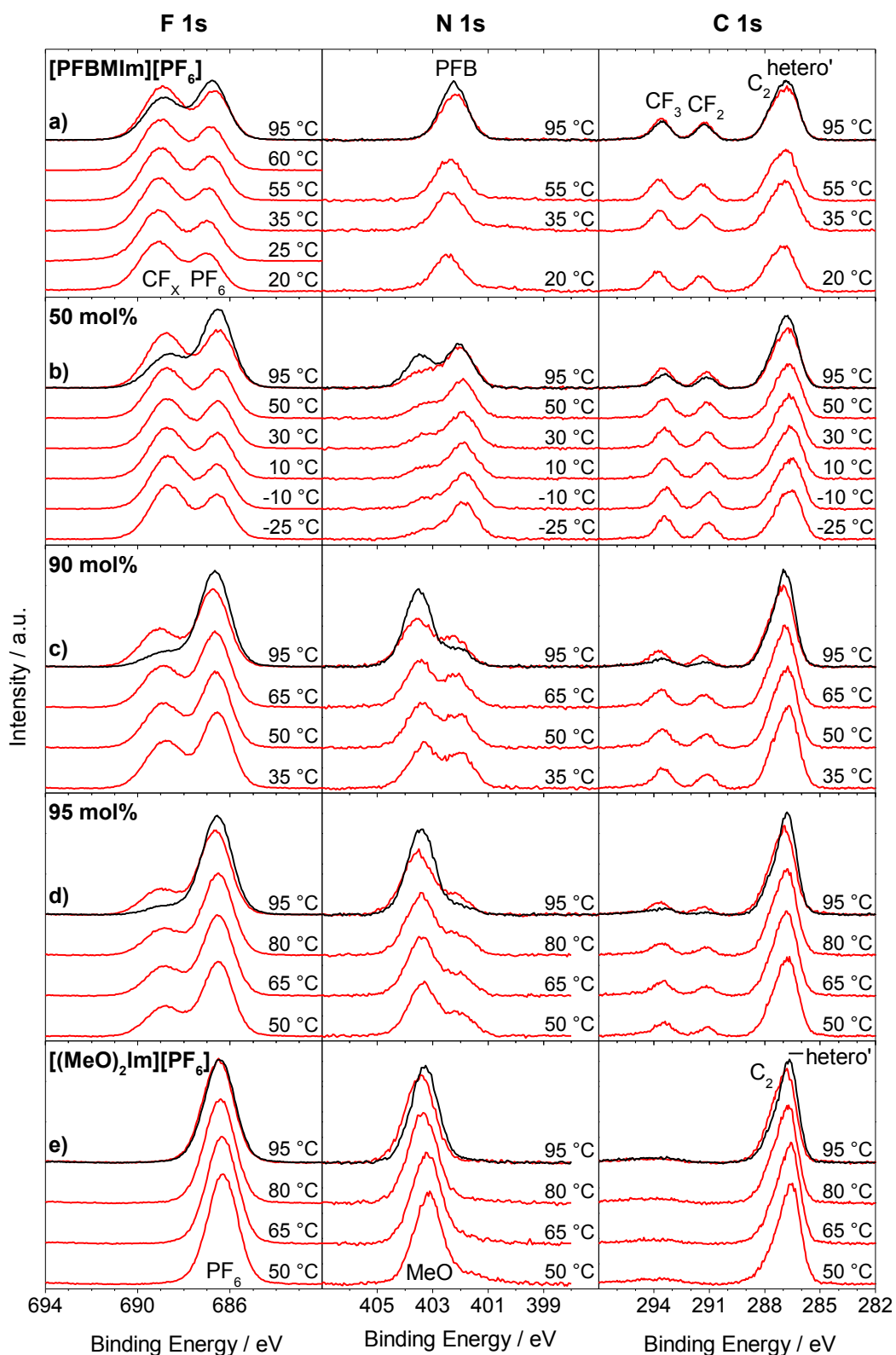
Figure 4.8: ARXP spectra recorded at 0° (black; only depicted for measurements at 95 °C) and 80° (red) emission of a) neat [PFBMIm][PF$_6$], b) – d) mixtures of [(MeO)$_2$Im][PF$_6$] and [PFBMIm][PF$_6$] at molar ratios of b) 50 mol% [(MeO)$_2$Im][PF$_6$], c) 90 mol% [(MeO)$_2$Im][PF$_6$] and d) 95 mol% [(MeO)$_2$Im][PF$_6$], and e) neat [(MeO)$_2$Im][PF$_6$]: F 1s (left), N 1s (middle) and C 1s (right). The samples were cooled from 95 °C to lower temperatures. Adapted in part from [P4] under license CC BY 4.0.

Again, this is attributed to a difference in surface tension related to the two different cations. Several structural features are known to influence the surface tension. From literature,[86] it is known that the surface tension of an oxygen-functionalized IL, [Me(EG)$_2$C$_1$Im][Tf$_2$N], is higher compared to [C$_8$C$_1$Im][Tf$_2$N] which has a comparable side chain length. In general, for homologous series of ILs with the same anion, the shorter the alkyl chain the larger the surface tension[71, 86, 111, 133-135] and an IL containing a fluorinated chain exhibits a lower surface tension compared to its respective alkylated IL.[60, 130, 131] Therefore, it is assumed that the surface tension value of [PFBMIm][PF$_6$] is considerably lower than the one for [(MeO)$_2$Im][PF$_6$] resulting in the observed depletion of the [(MeO)$_2$Im]$^+$ cation with respect to the surface-enriched [PFBMIm]$^+$ cation.

With increasing [(MeO)$_2$Im][PF$_6$] content in the mixtures, the normalized ratio of F$_{CFx}$ and F$_{PF6}$ (full squares in Figure 4.9) indicates a higher degree of surface enrichment of the fluorinated chain of the [PFBMIm]$^+$ cation relative to the [PF$_6$]$^-$ anion bulk concentration. In 80° (red) emission, the ratio for neat [PFBMIm][PF$_6$] is ~1.8 which represents solely the enrichment of the fluorinated chain. Values larger than this, like for the mixtures presented here, suggest an additional enrichment of the [PFBMIm]$^+$ head group. Furthermore, the open triangles in Figure 4.9 represent the normalized ratio of N$_{PFB}$ and N$_{MeO}$ in 80° (red) emission revealing the relative position of the two cationic head groups with respect to each other. The higher the [(MeO)$_2$Im][PF$_6$] content in the mixture, the higher is the normalized ratio of N$_{PFB}$ and N$_{MeO}$, indicating a more pronounced depletion of the [(MeO)$_2$Im]$^+$ cation with respect to the surface-enriched [PFBMIm]$^+$ head group. This trend coincides with the trend observed for the F$_{CFx}$ and F$_{PF6}$ ratio but is less pronounced for the nitrogen data. While the N 1s spectra only show the relative enrichment of the head groups damped by the surface-enriched fluorinated chain, the F$_{CFx}$ peaks in the F 1s spectra are not damped by any species. Remarkably, the trends of the normalized ratios of F$_{CFx}$ and F$_{PF6}$ as well as of N$_{PFB}$ and N$_{MeO}$ are also detected in 0° (black) emission for the mixtures with 90 and 95 mol% [(MeO)$_2$Im][PF$_6$], i.e. the depletion of the [PF$_6$]$^-$ anion and the [(MeO)$_2$Im]$^+$ cation is not only present in the topmost layer but also takes place in the near-surface region. Similar segregation effects have been detected for other IL systems earlier.[54, 96, 137]
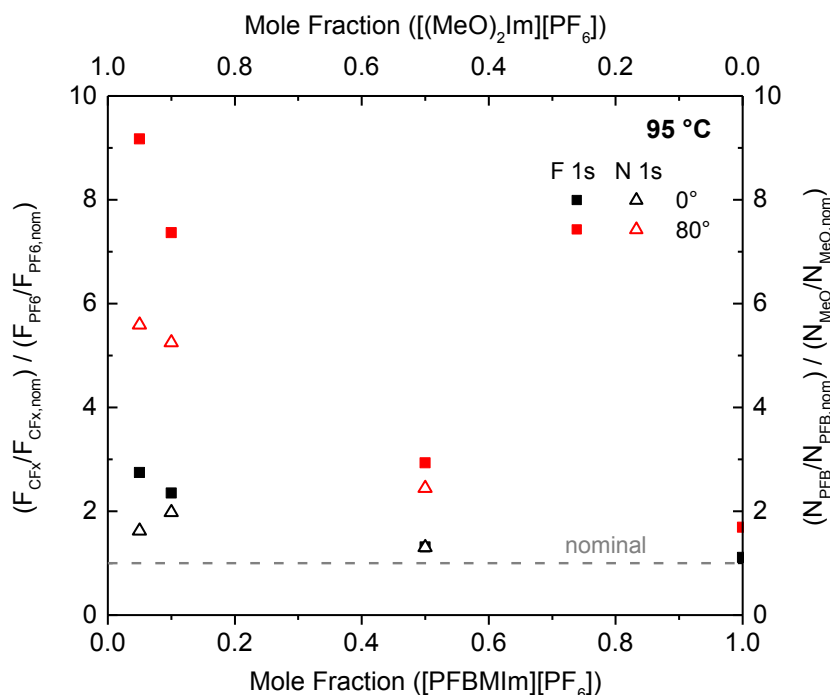
Figure 4.9: Normalized ratio of F_{CFx} and F_{PF6} (full squares; left axis) and normalized ratio of N_{PFB} and N_{MeO} (open triangles; right axis) at 0° (black) and 80° (red) emission. The gray dashed line indicates the nominal composition. The sample temperature was 95 °C. Adapted from [P4] under license CC BY 4.0.

Next, the 50, 90 and 95 mol% mixtures of $[(MeO)_2Im][PF_6]$ and $[PFBMIm][PF_6]$ are cooled to check for an even stronger surface enrichment of the $[PFBMIm]^+$ cation compared to the mixtures containing $[PFBMIm][PF_6]$ and $[C_nC_1Im][PF_6]$ described in Chapter 4.2.2. Since enrichment effects are most pronounced in 80° emission compared to 0°, only 80° spectra are discussed in the following. In Figure 4.8b – d, the F 1s, N 1s and C 1s spectra recorded at different temperatures are depicted and the normalized ratio of F_{CFx} and F_{PF6} (full squares) and of N_{PFB} and N_{MeO} (open triangles) are given in Figure 4.10b – d.

The solidification temperature of the mixtures is decreasing with decreasing $[(MeO)_2Im][PF_6]$ content. In general, when lowering the temperature of the 50, 90 and 95 mol% mixtures, the C_{CF3}, C_{CF2} and F_{CFx} peak intensities increase whereas the F_{PF6} intensity decreases to a lower extent. These changes correspond to an increase in the normalized ratio of F_{CFx} and F_{PF6} giving the highest value of ~12.2 at 50 °C for the mixture with 95 mol% $[(MeO)_2Im][PF_6]$. Also when cooling, a decrease of the N_{MeO} peak and an increase of the N_{PFB} peak are detected, resulting in a higher normalized ratio of N_{PFB} and N_{MeO} at low temperature. These results clearly show that the surface depletion of the $[PF_6]^-$

33

anion and the $[(MeO)_2Im]^+$ cation as well as the surface enrichment of the $[PFBMIm]^+$ cation with its fluorinated chain pointing towards the vacuum side is more pronounced the lower the temperature is. In other words, in contrast to the more random distribution of the $[PFBMIm]^+$ and $[(MeO)_2Im]^+$ cations at 95 °C, a more ordered surface is detected at lower temperature resulting from changes in the entropic term $-T \cdot \Delta S°$.
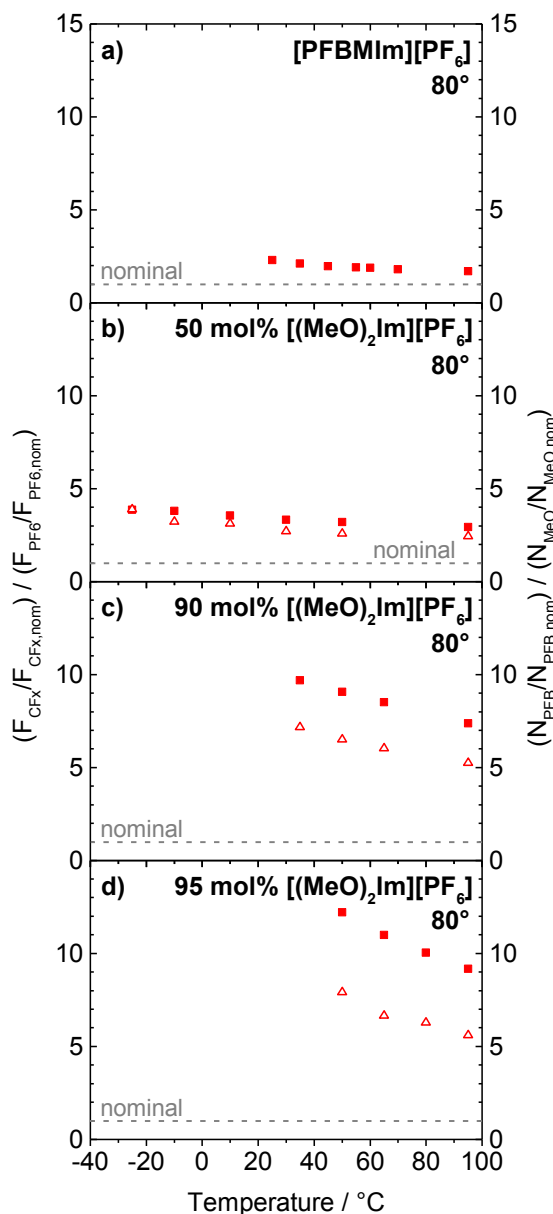
Figure 4.10: Ratio of the normalized F_{CFx} and F_{PF6} content (full squares; left axis) and of the normalized N_{PFB} and N_{MeO} content (open triangles; right axis) at 80° emission. The measurements were started at a sample temperature of 95 °C and subsequently cooled. a) Neat $[PFBMIm][PF_6]$, b) – d) mixtures of $[(MeO)_2Im][PF_6]$ and $[PFBMIm][PF_6]$ at molar ratios of b) 50 mol% $[(MeO)_2Im][PF_6]$, c) 90 mol% $[(MeO)_2Im][PF_6]$ and d) 95 mol% $[(MeO)_2Im][PF_6]$, and e) neat $[(MeO)_2Im][PF_6]$: Not shown due to the lack of F_{CFx} and N_{PFB} signals. The gray dashed lines indicate the nominal compositions. Adapted in part from [P4] under license CC BY 4.0.

Compared to the mixtures of [PFBMIm][PF$_6$] and [C$_4$C$_1$Im][PF$_6$][137] discussed in Chapter 4.2.2, a more pronounced enrichment of the fluorinated chain and the [PFBMIm]$^+$ head group is detected for the mixtures discussed in this chapter. For instance at 95 °C, the mixtures with 10 mol% [PFBMIm][PF$_6$] have a normalized ratio of F$_{CFx}$ and F$_{PF6}$ of ~7.4 or 3.5 when containing [(MeO)$_2$Im][PF$_6$] or [C$_4$C$_1$Im][PF$_6$], respectively.

4.3 Role of an Ionic Liquid Covering Graphene-Analogues[P5]

Exfoliated few layer two-dimensional (2D) antimonene and phosphorene in zero oxidation state are promising catalysts for the alkylation of acid-sensitive nucleophiles with esters under mild conditions, resulting in excellent selectivity and good yield. Preparing these pnictogens in $[C_4C_1Im][BF_4]$ results in suspended 2D materials. Moreover, catalytic reactions indicate that the IL efficiently protects these graphene-analogues from oxidation by air and water. To verify the zero oxidation state of antimonene and phosphorene and to confirm the protective effect of $[C_4C_1Im][BF_4]$, highly concentrated suspensions were prepared and spread on a clean gold foil by Vicent Lloret and Stefan Wild under inert glove box atmosphere. Subsequently, the suspensions were introduced into the DASSA setup after a short time period under ambient conditions. In this chapter, the XPS investigations will be discussed in detail. For further characterization and the catalytic activity studies performed by the co-authors, see the peer-reviewed article.[138]

In the following, only the 0° emission spectra of the antimonene (Sb 3d and O 1s region in Figure 4.11) and phosphorene (P 2p region in Figure 4.12) suspensions will be discussed. Starting with neat $[C_4C_1Im][BF_4]$, the survey spectrum shows the expected IL signals and additionally an O 1s (see also region spectrum in Figure 4.11–I) as well as a tiny Si 2p signal. Both most likely originate from a minor polysiloxane contamination of the glass ware used.[47, 114, 139] As expected, no signal is observed in the P 2p region shown in Figure 4.12–I.

The Sb 3d signals of the highly concentrated antimonene suspension are weak compared to the strong O 1s contamination peak (note the scaling factors in Figures 4.11 and 4.12). Therefore, a magnified spectrum is shown in green for antimonene (see Figure 4.11–II) revealing small non-oxidized, Sb^0, and oxidized, Sb^{ox}, Sb 3d peaks with Sb $3d_{5/2}$ peak positions of ~528.2 and 530.3 eV, respectively. For the phosphorene suspension, only one phosphorus species is detected in the P 2p region as small peak at ~130.6 eV in Figure 4.12–II, corresponding to non-oxidized phosphorus, P^0. The absence of a signal of oxidized phosphorus, P^{ox}, expected between 132 and 137 eV[140] confirms the protecting effect of $[C_4C_1Im][BF_4]$ for this pnictogen.
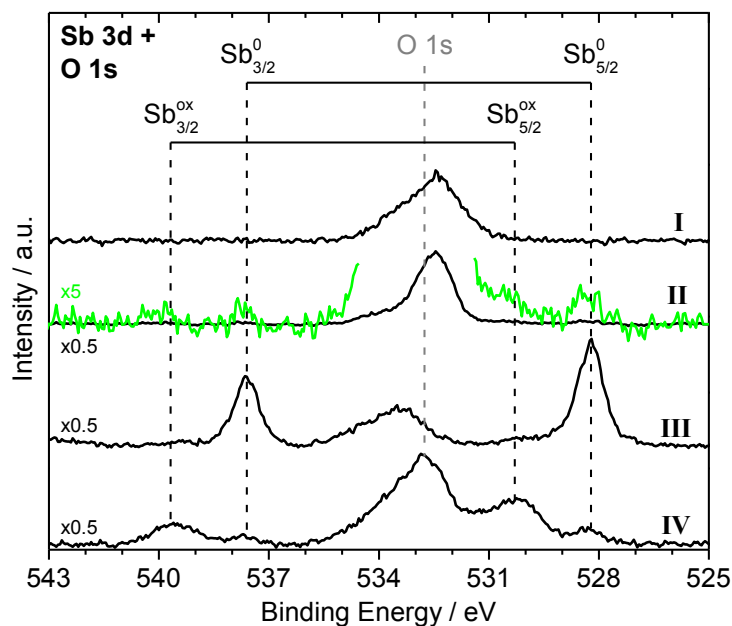
Figure 4.11: Sb 3d spectra including the O 1s peak of neat $[C_4C_1Im][BF_4]$ (I), a highly concentrated antimonene suspension (II) with a magnification (green) to see the small peaks of non-oxidized and oxidized antimony, after removal of most of the $[C_4C_1Im][BF_4]$ by heating (III) and after exposure to air for about one day (IV). The spectra are offset for clarity. Adapted from [P5] under license CC BY 4.0.

Heating both suspensions above 150 °C for about one hour under UHV leads to a significant increase in the XP intensity of the non-oxidized antimonene and phosphorene signals in Figures 4.11–III and 4.12–III whereas the intensity of the IL related signals decreases drastically due to thermal IL desorption (and possibly some IL decomposition). This indicates that the majority of antimony and phosphorus in the 2D materials is in a zero oxidation state whereas the Sb^{ox} is indeed a minority species in the antimonene suspension.

The heated samples (with a considerably decreased IL content) are then removed from the UHV chamber and kept under ambient conditions for about one day. Subsequent XPS measurements revealed that due to the removal of most of the $[C_4C_1Im][BF_4]$, indeed its protective effect of the pnictogens against oxidation is lost: A considerable amount of oxidized antimony and phosphorus is detected in the respective sample after exposure to atmosphere. For the Sb $3d_{5/2}$ peak of the non-oxidized Sb^0 species at ~528.3 eV a pronounced decrease is detected while the peak of the oxidized Sb^{ox} species at ~530.2 eV has gained intensity (see Figure 4.11–IV). For the phosphorene sample, the non-oxidized P^0 species is still detected at ~130.7 eV, however, at higher binding energy a broad peak between 132 and 137 eV is observed corresponding to oxidized phosphorus, P^{ox}, highlighted in green in Figure 4.12–IV.
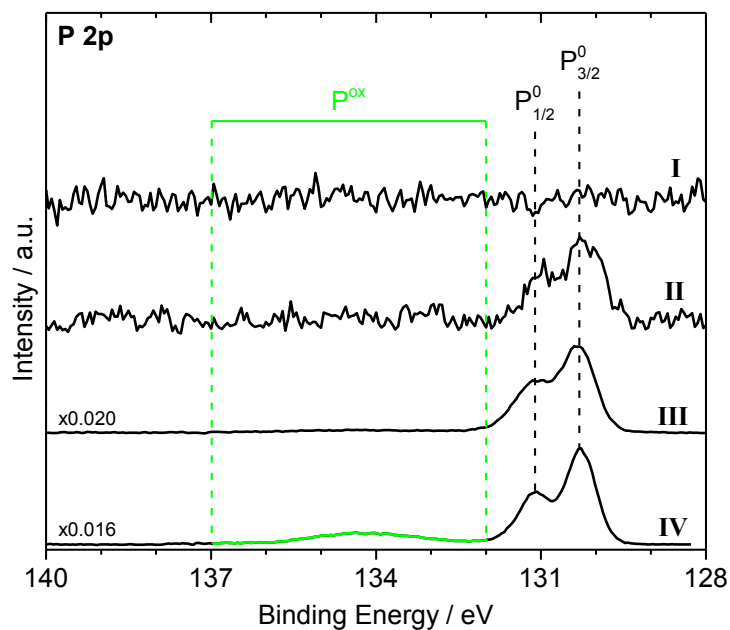
Figure 4.12: P 2p spectra of neat $[C_4C_1Im][BF_4]$ (I), a highly concentrated phosphorene suspension (II), after removal of most of the $[C_4C_1Im][BF_4]$ by heating (III) and after exposure to air for about one day (IV). The spectra are offset for clarity. Adapted from [P5] under license CC BY 4.0.

5 Summary

This thesis focuses on the surface investigations of neat ionic liquids (ILs) and of binary IL mixtures, particularly mixtures involving functionalized imidazolium-based cations. The investigations are performed by means of angle-resolved X-ray photoelectron spectroscopy (ARXPS), a surface-sensitive ultra-high vacuum (UHV) technique, accessing the first 7 to 9 nm under 0° emission and the topmost 1 to 1.5 nm under 80° emission. Intensity changes of the IL signals with the emission angle directly reflect surface enrichment and depletion of ions as well as molecular orientation effects in the outermost surface layer.

The first part of this thesis is dedicated to the correlation of the surface composition with the surface tension according to the concept of molecular group contributions at the outer surface introduced by Langmuir.[104, 105] Combining ARXPS measurements and molecular dynamics (MD) simulations, the composition of $[C_nC_1Im][Tf_2N]$ ILs (with $n = 2$, 4, 6, 8, 10 and 12) close to the surface is investigated by comparing the surface enrichment of the alkyl chain with respect to the cationic head group along the IL series.[106] While an earlier fit model for ARXPS C 1s peaks worked well qualitatively, a correction involving the attenuation of the nitrogen signals of the imidazolium ring is crucial for the quantification of the C_{hetero} and C_{alkyl} signals at 80°. Taking the corresponding 0° and 80° information depth into account, a very good agreement between ARXPS measurements and MD simulations is obtained. Finally, the surface tension values are derived from the simulated outer surface composition allowing for the comparison with experimental data.[86] An emission angle of 87.5° might be surface-sensitive enough to limit ARXPS signals to the molecular groups at the outer surface.

As main topic of this thesis, enrichment and depletion effects at the IL/vacuum interface are investigated in various IL mixtures, containing functionalized imidazolium-based cations. The cation of neat $[(MeO)_2Im][PF_6]$, a methoxy-functionalized IL containing oxygen atoms directly bound to each nitrogen atom of the imidazolium ring, reveals a different electronic structure induced by the oxygen atoms. The resulting more positively charged imidazolium ring exhibits characteristic XP peaks located at higher binding energy compared to $[C_nC_1Im]^+$ cations, *e.g.* in the N 1s spectrum a shift of the N_{MeO} peak of ~+1.4 eV in contrast to the N_{Im} peak is detected.[96] The chemical shift of the nitrogen atoms of the $[(MeO)_2Im]^+$ cation facilitates the investigation of enrichment and depletion effects in IL mixtures. In the liquid state, no surface enrichment or depletion

effects are detected for neat [(MeO)$_2$Im][PF$_6$].[96, 136] The other investigated functionalized IL is [PFBMIm][PF$_6$], possessing a butyl chain with its two terminal carbon atoms fluorinated. At 95 °C, a surface enrichment of the fluorinated chain with respect to the other IL moieties is observed.[136, 137]

Mixing the functionalized ILs with each other[136] and with non-functionalized [C$_n$C$_1$Im][PF$_6$] (with n = 2, 4 and 8) or [C$_8$C$_1$Im][Tf$_2$N][96, 137] results in distinct XP peaks for each ion, which allows for obtaining detailed information about the relative positions of the cation and the anion or the respective cations and anions to each other. It is proposed that the IL with the lower surface tension is preferentially enriched at the IL/vacuum interface. At 95 °C, one major result is that the fluorinated chain of mixtures containing [PFBMIm][PF$_6$] is surface-enriched. This is more pronounced the lower the [PFBMIm][PF$_6$] content in mixtures with [(MeO)$_2$Im][PF$_6$] and [C$_n$C$_1$Im][PF$_6$] (with n = 2, 4 and 8) is.[136, 137] Furthermore, the shorter the alkyl chain length, n, of [C$_n$C$_1$Im][PF$_6$] in the mixtures with [PFBMIm][PF$_6$], the more pronounced is the enrichment of the fluorinated chain, which is attributed to a competing effect of the long alkyl chains with the shorter fluorinated chains at the surface. In contrast, the cationic head group of [(MeO)$_2$Im][PF$_6$] is depleted from the topmost layers in mixtures with [C$_8$C$_1$Im][PF$_6$], [C$_8$C$_1$Im][Tf$_2$N] and [PFBMIm][PF$_6$].[96, 136] A non-stoichiometric distribution of cations and anions of several mixtures is not only observed in 80° but also in the more bulk-sensitive 0° measurements revealing that in the near-surface region enrichment and depletion effects are present. In catalytic processes, *e.g.* Supported Ionic Liquid Phase (SILP) catalysis, a lower temperature can be desirable to achieve high equilibrium conversions.[73] To understand changes in the surface composition as a function of temperature, most of the aforementioned mixtures are investigated by means of temperature-dependent ARXPS from 95 °C to their onset of solidification. The surface enrichment of the fluorinated chain of the [PFBMIm]$^+$ cation with respect to the [PF$_6$]$^-$ anion is more pronounced, the lower the temperature resulting from a decrease in entropic contributions.

The last part of this thesis is dedicated to the investigation of the catalytically active two-dimensional (2D) materials antimonene and phosphorene dispersed in [C$_4$C$_1$Im][BF$_4$] with focus on the protection against oxidation by the IL.[138] In highly concentrated suspensions, XPS reveals that the majority of the synthesized antimonene and phosphorene is in a zero oxidation state. Thus, the IL protects the 2D materials from oxidation by air

and water. If the protective $[C_4C_1Im][BF_4]$ film is removed and the samples are kept under ambient conditions for one day, pronounced oxidation of antimonene and phosphorene are observed.

6 Zusammenfassung

Diese Dissertation befasst sich mit der Oberflächenuntersuchung reiner Ionischer Flüssigkeiten (engl. ionic liquids, ILs) und deren binären Mischungen, die funktionalisierte Imidazolium-basierte Kationen enthalten. Die Untersuchungen werden mittels winkelaufgelöster Röntgenphotoelektronenspektroskopie (engl. angle-resolved X-ray photoelectron spectroscopy, ARXPS), einer oberflächenempfindlichen Messmethode im Ultrahochvakuum, durchgeführt. Dies ermöglicht unter einem Emissionswinkel von 0° die ersten 7 bis 9 nm sowie unter 80° die äußersten 1 bis 1,5 nm einer Probe zu untersuchen. Der Vergleich der unter 0° und 80° detektierten IL-Signalintensitäten lässt direkte Rückschlüsse auf Oberflächenanreicherung und -abreicherung von Ionen zu und gibt Informationen über molekulare Orientierungseffekte in der äußersten Oberflächenschicht.

Der erste Teil dieser Dissertation behandelt den Zusammenhang der IL-Oberflächenzusammensetzung und der Oberflächenspannung gemäß des Konzeptes nach Langmuir zum Beitrag der Molekülgruppen der äußersten Oberfläche zur Oberflächenspannung.[104, 105] Durch das Kombinieren von ARXPS-Messungen und Moleculardynamik-Simulationen (MD) wird die Oberflächenzusammensetzung der $[C_nC_1Im][Tf_2N]$-ILs (mit $n = 2, 4, 6, 8, 10$ und 12) untersucht, indem entlang dieser IL-Reihe die Anreicherung der Alkylkette im Verhältnis zu den kationischen Kopfgruppen verglichen wird.[106] Da ein früheres Fitmodell der ARXPS C 1s-Signale nur qualitative Ergebnisse lieferte, wird für die Quantifizierung der C_{hetero}- und C_{alkyl}-Signale der 80°-Spektren eine Korrektur über die Dämpfung der Stickstoffsignale des Imidazoliumrings eingeführt. Unter Berücksichtigung der entsprechenden Informationstiefen unter 0° und 80°, ergibt sich eine gute Übereinstimmung zwischen den ARXPS-Messungen und den MD-Simulationen. Darüber hinaus wird die Oberflächenspannung mittels der simulierten Oberflächenzusammensetzung abgeleitet und mit experimentellen Werten verglichen.[86] Ein Emissionswinkel von 87,5° wäre wahrscheinlich ausreichend oberflächensensitiv, um mittels ARXPS nur die äußerste Oberfläche zu untersuchen.

Schwerpunkt dieser Dissertation sind Oberflächenanreicherungseffekte und -abreicherungseffekte an der IL/Vakuum-Grenzfläche in verschiedenen IL-Mischungen, die funktionalisierte Imidazolium-basierte Kationen enthalten. $[(MeO)_2Im][PF_6]$ ist eine methoxy-funktionalisierte IL, deren Sauerstoffatome direkt an die beiden Stickstoffatome des Imidazoliumrings gebunden sind. Diese Sauerstoffatome verändern die elektronische

Struktur des Kations. Der Imidazoliumring des $[(MeO)_2Im]^+$-Kations ist im Vergleich zu dem der $[C_nC_1Im]^+$-Kationen positiver geladen, woraus charakteristische XP-Peaks bei höheren Bindungsenergien resultieren. Im N 1s-Spektrum ist, im Vergleich zum N_{Im}-Peak, das N_{MeO}-Signal beispielsweise um ~+1,4 eV verschoben.[96] Diese chemische Verschiebung der Stickstoffatome des $[(MeO)_2Im]^+$-Kations erleichtert die Untersuchung von Oberflächenanreicherungseffekten und -abreicherungseffekten in IL-Mischungen. Die Spektren des reinen, flüssigen $[(MeO)_2Im][PF_6]$ zeigen keine Oberflächenaktivität.[96, 136] Des Weiteren wird die funktionalisierte $[PFBMIm][PF_6]$-IL untersucht, deren beide endständigen Kohlenstoffatome der Butylkette vollständig fluoriert sind. Im Vergleich zu den anderen IL-„Teilen", ist die fluorierte Kette bei 95 °C an der Oberfläche angereichert.[136, 137]

Mischungen der beiden funktionalisierten ILs miteinander[136] sowie von einer funktionalisierten IL mit den nicht-funktionalisierten ILs $[C_nC_1Im][PF_6]$ (mit $n = 2$, 4 und 8) oder mit $[C_8C_1Im][Tf_2N]$[96, 137] resultieren in charakteristischen XP-Signalen, welche die Unterscheidung der Ionen ermöglicht. Daraus können Schlussfolgerungen über die relative Position der jeweiligen Kationen und Anionen zueinander gezogen werden. Es wird angenommen, dass sich die IL mit der kleineren Oberflächenspannung bevorzugt an der IL/Vakuum-Grenzfläche befindet. Eines der Hauptergebnisse bei 95 °C ist, dass sich die fluorierte Kette der $[PFBMIm][PF_6]$-Mischungen an der Oberfläche anreichert. In den Mischungen mit $[(MeO)_2Im][PF_6]$ und $[C_nC_1Im][PF_6]$ (mit $n = 2$, 4 und 8) ist dieser Anreicherungseffekt umso ausgeprägter, je kleiner der Anteil des $[PFBMIm][PF_6]$ in der Mischung ist.[136, 137] Des Weiteren hat die Länge der Alkylkette, n, einen Einfluss auf die Anreicherung der fluorierten Kette. Je kürzer die Alkylkette der $[C_nC_1Im][PF_6]$-IL in der Mischung mit $[PFBMIm][PF_6]$, desto stärker reichert sich die fluorierte Kette an. Dies wird auf einen konkurrierenden Effekt der langen Alkylkette mit der kürzeren fluorierten Kette an der Oberfläche zurückgeführt. Im Gegensatz dazu wird die Abreicherung der kationischen Kopfgruppe des $[(MeO)_2Im][PF_6]$ aus der obersten Lage der Mischungen mit $[C_8C_1Im][PF_6]$, $[C_8C_1Im][Tf_2N]$ und $[PFBMIm][PF_6]$ detektiert.[96, 136] In einigen Mischungen werden nicht-stöchiometrische Verteilungen der Kationen und Anionen nicht nur an der Oberfläche unter 80°, sondern auch unter einem Emissionswinkel von 0° beobachtet. Dies zeigt, dass Anreicherungs- und Abreicherungseffekte im oberflächennahen Bereich vorliegen. Bei katalytischen Prozessen, wie beispielsweise SILP-Systemen (Supported Ionic Liquid Phase), kann eine niedrigere Prozesstemperatur erwünscht sein,

um einen höheren Gleichgewichtsumsatz zu erzielen.[73] Temperaturabhängige Änderungen der Oberflächenzusammensetzung einiger der zuvor genannten IL-Mischungen werden mittels temperaturabhängiger ARXPS-Messung von 95 °C bis zum Beginn der Verfestigung der Mischungen untersucht. Mit abnehmender Temperatur ist eine Zunahme der Oberflächenanreicherung der fluorierten Kette im Verhältnis zum $[PF_6]^-$-Anion zu beobachten, was durch die Abnahme des Entropiebeitrages erklärt werden kann.

Der letzte Teil dieser Dissertation widmet sich der Untersuchung der fein verteilten katalytisch aktiven zweidimensionalen (2D) Materialien Antimonen und Phosphoren in $[C_4C_1Im][BF_4]$.[138] Der Fokus dieser Untersuchung ist die schützende Wirkung der IL, um Oxidation zu verhindern. XPS zeigt, dass der größte Teil des synthetisierten Antimonens und Phosphorens in hoch konzentrierten Suspensionen im Oxidationszustand Null vorliegt. Das bedeutet, dass die IL die 2D-Materialien vor der Oxidation durch Luft und Wasser schützt. Wenn ein Großteil des schützenden $[C_4C_1Im][BF_4]$-Films entfernt wird, führt das eintägige Lagern der Proben unter Umgebungsbedingungen zur Oxidation des Antimonens und des Phosphorens.

7 Literature

[1]   H.-P. Steinrück, P. Wasserscheid, Ionic Liquids in Catalysis, *Catal. Lett.* **2015**, *145*, 380-397.

[2]   A. S. L. Gouveia, C. E. S. Bernardes, E. I. Lozinskaya, A. S. Shaplov, J. N. Canongia Lopes, I. M. Marrucho, Neat ionic liquids *versus* ionic liquid mixtures: a combination of experimental data and molecular simulation, *Phys. Chem. Chem. Phys.* **2019**, *21*, 23305-23309.

[3]   T. L. Greaves, D. F. Kennedy, Y. Shen, A. Hawley, G. Song, C. J. Drummond, Fluorous protic ionic liquids exhibit discrete segregated nano-scale solvent domains and form new populations of nano-scale objects upon primary alcohol addition, *Phys. Chem. Chem. Phys.* **2013**, *15*, 7592-7598.

[4]   M. L. Ferreira, M. J. Pastoriza-Gallego, J. M. M. Araújo, J. N. Canongia Lopes, L. P. N. Rebelo, M. M. Piñeiro, K. Shimizu, A. B. Pereiro, Influence of Nanosegregation on the Phase Behavior of Fluorinated Ionic Liquids, *J. Phys. Chem. C* **2017**, *121*, 5415-5427.

[5]   P. Sun, D. W. Armstrong, Ionic liquids in analytical chemistry, *Anal. Chim. Acta* **2010**, *661*, 1-16.

[6]   T. Torimoto, T. Tsuda, K.-i. Okazaki, S. Kuwabata, New Frontiers in Materials Science Opened by Ionic Liquids, *Adv. Mater.* **2010**, *22*, 1196-1221.

[7]   N. V. Plechkova, K. R. Seddon, Applications of ionic liquids in the chemical industry, *Chem. Soc. Rev.* **2008**, *37*, 123-150.

[8]   D. W. Bruce, C. P. Cabry, J. N. Canongia Lopes, M. L. Costen, L. D'Andrea, I. Grillo, B. C. Marshall, K. G. McKendrick, T. K. Minton, S. M. Purcell, S. Rogers, J. M. Slattery, K. Shimizu, E. Smoll, M. A. Tesa-Serrate, Nanosegregation and Structuring in the Bulk and at the Surface of Ionic-Liquid Mixtures, *J. Phys. Chem. B* **2017**, *121*, 6002-6020.

[9]   H. Niedermeyer, J. P. Hallett, I. J. Villar-Garcia, P. A. Hunt, T. Welton, Mixtures of ionic liquids, *Chem. Soc. Rev.* **2012**, *41*, 7780-7802.

[10]   M. T. Clough, C. R. Crick, J. Gräsvik, P. A. Hunt, H. Niedermeyer, T. Welton, O. P. Whitaker, A physicochemical investigation of ionic liquid mixtures, *Chem. Sci.* **2015**, *6*, 1101-1114.

[11]   G. Chatel, J. F. B. Pereira, V. Debbeti, H. Wang, R. D. Rogers, Mixing ionic liquids – "simple mixtures" or "double salts"?, *Green Chem.* **2014**, *16*, 2051-2083.

[12]   J. C. Forgie, S. El Khakani, D. D. MacNeil, D. Rochefort, Electrochemical characterisation of a lithium-ion battery electrolyte based on mixtures of carbonates with a ferrocene-functionalised imidazolium electroactive ionic liquid, *Phys. Chem. Chem. Phys.* **2013**, *15*, 7713-7721.

[13]   P. M. Bayley, A. S. Best, D. R. MacFarlane, M. Forsyth, The effect of coordinating and non-coordinating additives on the transport properties in ionic liquid electrolytes for lithium batteries, *Phys. Chem. Chem. Phys.* **2011**, *13*, 4632-4640.

[14]   S. Ferrari, E. Quartarone, C. Tomasi, D. Ravelli, S. Protti, M. Fagnoni, P. Mustarelli, Alkoxy substituted imidazolium-based ionic liquids as electrolytes for lithium batteries, *J. Power Sources* **2013**, *235*, 142-147.

[15]   D. S. Silvester, Recent advances in the use of ionic liquids for electrochemical sensing, *Analyst* **2011**, *136*, 4871-4882.

[16]   T. Yasuda, M. Watanabe, Protic ionic liquids: Fuel cell applications, *MRS Bull.* **2013**, *38*, 560-566.

[17]   M. Díaz, A. Ortiz, I. Ortiz, Progress in the use of ionic liquids as electrolyte membranes in fuel cells, *J. Membr. Sci.* **2014**, *469*, 379-396.

[18]   S. Tsuzuki, T. Umecky, H. Matsumoto, W. Shinoda, M. Mikami, Interactions of Perfluoroalkyltrifluoroborate Anions with Li Ion and Imidazolium Cation: Effects of Perfluoroalkyl Chain on Motion of Ions in Ionic Liquids, *J. Phys. Chem. B* **2010**, *114*, 11390-11396.

[19]   M. J. Trujillo-Rodríguez, H. Nan, M. Varona, M. N. Emaus, I. D. Souza, J. L. Anderson, Advances of Ionic Liquids in Analytical Chemistry, *Anal. Chem.* **2019**, *91*, 505-531.

[20]   M. S. Miran, T. Yasuda, M. A. B. H. Susan, K. Dokko, M. Watanabe, Binary Protic Ionic Liquid Mixtures as a Proton Conductor: High Fuel Cell Reaction Activity and Facile Proton Transport, *J. Phys. Chem. C* **2014**, *118*, 27631-27639.

[21]   S. Fang, L. Qu, D. Luo, S. Shen, L. Yang, S.-i. Hirano, Novel mixtures of ether-functionalized ionic liquids and non-flammable methylperfluorobutylether as safe electrolytes for lithium metal batteries, *RSC Adv.* **2015**, *5*, 33897-33904.

[22]   M. Watanabe, M. L. Thomas, S. Zhang, K. Ueno, T. Yasuda, K. Dokko, Application of Ionic Liquids to Energy Storage and Conversion Materials and Devices, *Chem. Rev.* **2017**, *117*, 7190-7239.

[23]   H. Xiao, Ionic Liquid Lubricants: Basics and Applications, *Tribol. Trans.* **2017**, *60*, 20-30.

[24]   Q. Q. Baltazar, S. K. Leininger, J. L. Anderson, Binary ionic liquid mixtures as gas chromatography stationary phases for improving the separation selectivity of alcohols and aromatic compounds, *J. Chromatogr. A* **2008**, *1182*, 119-127.

[25]   C. F. Poole, S. K. Poole, Ionic liquid stationary phases for gas chromatography, *J. Sep. Sci.* **2011**, *34*, 888-900.

[26]   L. Zhou, J. Fan, X. Shang, CO_2 Capture and Separation Properties in the Ionic Liquid 1-n-Butyl-3-Methylimidazolium Nonafluorobutylsulfonate, *Materials* **2014**, *7*, 3867-3880.

[27]   F. Meischl, M. Harder, C. G. Kirchler, J. Kremser, C. W. Huck, G. K. Bonn, M. Rainer, Novel asymmetric 1,3-di(alkyloxy)imidazolium based ionic liquids for liquid-phase microextraction of selected analgesics and estrogens from aqueous samples, *J. Mol. Liq.* **2019**, *289*, 111157.

[28]   R. I. Canales, J. F. Brennecke, Comparison of Ionic Liquids to Conventional Organic Solvents for Extraction of Aromatics from Aliphatics, *J. Chem. Eng. Data* **2016**, *61*, 1685-1699.

[29]   A. Bösmann, L. Datsevich, A. Jess, A. Lauter, C. Schmitz, P. Wasserscheid, Deep desulfurization of diesel fuel by extraction with ionic liquids, *Chem. Commun.* **2001**, 2494-2495.

[30] R.-S. Zhao, X. Wang, F.-W. Li, S.-S. Wang, L.-L. Zhang, C.-G. Cheng, Ionic liquid/ionic liquid dispersive liquid–liquid microextraction, *J. Sep. Sci.* **2011**, *34*, 830-836.

[31] U. Kernchen, B. Etzold, W. Korth, A. Jess, Solid Catalyst with Ionic Liquid Layer (SCILL) – A New Concept to Improve Selectivity Illustrated by Hydrogenation of Cyclooctadiene, *Chem. Eng. Technol.* **2007**, *30*, 985-994.

[32] J. van den Broeke, F. Winter, B.-J. Deelman, G. van Koten, A Highly Fluorous Room-Temperature Ionic Liquid Exhibiting Fluorous Biphasic Behavior and Its Use in Catalyst Recycling, *Org. Lett.* **2002**, *4*, 3851-3854.

[33] Y. Tsukada, K. Iwamoto, H. Furutani, Y. Matsushita, Y. Abe, K. Matsumoto, K. Monda, S. Hayase, M. Kawatsura, T. Itoh, Preparation of novel hydrophobic fluorine-substituted-alkyl sulfate ionic liquids and application as an efficient reaction medium for lipase-catalyzed reaction, *Tetrahedron Lett.* **2006**, *47*, 1801-1804.

[34] S. Marullo, C. Rizzo, F. D'Anna, Task-Specific Organic Salts and Ionic Liquids Binary Mixtures: A Combination to Obtain 5-Hydroxymethylfurfural From Carbohydrates, *Front. Chem.* **2019**, *7*, 134.

[35] S. Zhang, J. Zhang, Y. Zhang, Y. Deng, Nanoconfined Ionic Liquids, *Chem. Rev.* **2017**, *117*, 6755-6833.

[36] H.-P. Steinrück, J. Libuda, P. Wasserscheid, T. Cremer, C. Kolbeck, M. Laurin, F. Maier, M. Sobota, P. S. Schulz, M. Stark, Surface Science and Model Catalysis with Ionic Liquid-Modified Materials, *Adv. Mater.* **2011**, *23*, 2571-2587.

[37] C. P. Mehnert, E. J. Mozeleski, R. A. Cook, Supported ionic liquid catalysis investigated for hydrogenation reactions, *Chem. Commun.* **2002**, 3010-3011.

[38] A. Riisager, R. Fehrmann, M. Haumann, B. S. K. Gorle, P. Wasserscheid, Stability and Kinetic Studies of Supported Ionic Liquid Phase Catalysts for Hydroformylation of Propene, *Ind. Eng. Chem. Res.* **2005**, *44*, 9853-9859.

[39] J. M. Marinkovic, A. Riisager, R. Franke, P. Wasserscheid, M. Haumann, Fifteen Years of Supported Ionic Liquid Phase-Catalyzed Hydroformylation: Material and Process Developments, *Ind. Eng. Chem. Res.* **2019**, *58*, 2409-2420.

[40] T. Cremer, L. Wibmer, S. Krick Calderón, A. Deyko, F. Maier, H.-P. Steinrück, Interfaces of ionic liquids and transition metal surfaces—adsorption, growth, and thermal ractions of ultrathin $[C_1C_1Im][Tf_2N]$ films on metallic and oxidised Ni(111) surfaces, *Phys. Chem. Chem. Phys.* **2012**, *14*, 5153-5163.

[41] M. B. Oliveira, M. Domínguez-Pérez, O. Cabeza, J. A. Lopes-da-Silva, M. G. Freire, J. A. P. Coutinho, Surface tensions of binary mixtures of ionic liquids with bis(trifluoromethylsulfonyl)imide as the common anion, *J. Chem. Thermodynamics* **2013**, *64*, 22-27.

[42] H.-P. Steinrück, Recent developments in the study of ionic liquid interfaces using X-ray photoelectron spectroscopy and potential future directions, *Phys. Chem. Chem. Phys.* **2012**, *14*, 5010-5029.

[43] C. Kolbeck, A. Deyko, T. Matsuda, F. T. U. Kohler, P. Wasserscheid, F. Maier, H.-P. Steinrück, Temperature-Dependent Surface-Enrichment Effects of Imidazolium-Based Ionic Liquids, *ChemPhysChem* **2013**, *14*, 3726-3730.

[44] M. Lexow, B. S. J. Heller, F. Maier, H.-P. Steinrück, Anion Exchange at the Liquid/Solid Interface of Ultrathin Ionic Liquid Films on Ag(111), *ChemPhysChem* **2018**, *19*, 2978-2984.

[45] M. Lexow, B. S. J. Heller, G. Partl, R. G. Bhuin, F. Maier, H.-P. Steinrück, Cation Exchange at the Interfaces of Ultrathin Films of Fluorous Ionic Liquids on Ag(111), *Langmuir* **2019**, *35*, 398-405.

[46] I. J. Villar-Garcia, S. Fearn, G. F. De Gregorio, N. L. Ismail, F. J. V. Gschwend, A. J. S. McIntosh, K. R. J. Lovelock, The ionic liquid–vacuum outer atomic surface: a low-energy ion scattering study, *Chem. Sci.* **2014**, *5*, 4404-4418.

[47] J. M. Gottfried, F. Maier, J. Rossa, D. Gerhard, P. S. Schulz, P. Wasserscheid, H.-P. Steinrück, Surface Studies on the Ionic Liquid 1-Ethyl-3-Methylimidazolium Ethylsulfate Using X-ray Photoelectron Spectroscopy (XPS), *Z. Phys. Chem.* **2006**, *220*, 1439-1453.

[48] J. J. Hettige, W. D. Amith, E. W. Castner, Jr., C. J. Margulis, Ionic Liquids with Symmetric Diether Tails: Bulk and Vacuum-Liquid Interfacial Structures, *J. Phys. Chem. B* **2017**, *121*, 174-179.

[49] I. S. Martinez, S. Baldelli, On the Arrangement of Ions in Imidazolium-Based Room Temperature Ionic Liquids at the Gas−Liquid Interface, Using Sum Frequency Generation, Surface Potential, and Surface Tension Measurements, *J. Phys. Chem. C* **2010**, *114*, 11564-11575.

[50] K. Nakajima, M. Miyashita, M. Suzuki, K. Kimura, Surface structures of binary mixtures of imidazolium-based ionic liquids using high-resolution Rutherford backscattering spectroscopy and time of flight secondary ion mass spectroscopy, *J. Chem. Phys.* **2013**, *139*, 224701.

[51] K. Nakajima, S. Nakanishi, M. Lísal, K. Kimura, Surface structures of binary mixture of ionic liquids, *J. Mol. Liq.* **2017**, *230*, 542-549.

[52] F. Maier, T. Cremer, C. Kolbeck, K. R. J. Lovelock, N. Paape, P. S. Schulz, P. Wasserscheid, H.-P. Steinrück, Insights into the surface composition and enrichment effects of ionic liquid mixtures, *Phys. Chem. Chem. Phys.* **2010**, *12*, 1905-1915.

[53] C. Kolbeck, I. Niedermaier, A. Deyko, K. R. J. Lovelock, N. Taccardi, W. Wei, P. Wasserscheid, F. Maier, H.-P. Steinrück, Influence of Substituents and Functional Groups on the Surface Composition of Ionic Liquids, *Chem. Eur. J.* **2014**, *20*, 3954-3965.

[54] Y. Zhang, Y. Khalifa, E. J. Maginn, J. T. Newberg, Anion Enhancement at the Liquid–Vacuum Interface of an Ionic Liquid Mixture, *J. Phys. Chem. C* **2018**, *122*, 27392-27401.

[55] S. Palchowdhury, B. L. Bhargava, Segregation of ions at the interface: molecular dynamics studies of the bulk and liquid–vapor interface structure of equimolar binary mixtures of ionic liquids, *Phys. Chem. Chem. Phys.* **2015**, *17*, 19919-19928.

[56] S. Palchowdhury, B. L. Bhargava, Surface Structure and Dynamics of Ions at the Liquid–Vapor Interface of Binary Ionic Liquid Mixtures: Molecular Dynamics Studies, *J. Phys. Chem. B* **2016**, *120*, 5430-5441.

[57] C. Ridings, G. G. Warr, G. G. Andersson, Surface Ordering in Binary Mixtures of Protic Ionic Liquids, *J. Phys. Chem. Lett.* **2017**, *8*, 4264-4267.

[58] F. Wu, W. V. Karunaratne, C. J. Margulis, Ionic Liquid Mixture at the Vacuum Interface and the Peaks and Antipeaks Analysis of X-ray Reflectivity, *J. Phys. Chem. C* **2019**, *123*, 4914-4925.

[59] I. J. Villar-Garcia, S. Fearn, N. L. Ismail, A. J. S. McIntosh, K. R. J. Lovelock, Fine tuning the ionic liquid–vacuum outer atomic surface using ion mixtures, *Chem. Commun.* **2015**, *51*, 5367-5370.

[60] E. J. Smoll, Jr., M. A. Tesa-Serrate, S. M. Purcell, L. D'Andrea, D. W. Bruce, J. M. Slattery, M. L. Costen, T. K. Minton, K. G. McKendrick, Determining the composition of the vacuum–liquid interface in ionic-liquid mixtures, *Faraday Discuss.* **2018**, *206*, 497-522.

[61] R. Souda, Surface segregation in binary mixtures of imidazolium-based ionic liquids, *Surf. Sci.* **2010**, *604*, 1694-1697.

[62] O. Höfft, S. Bahr, M. Himmerlich, S. Krischok, J. A. Schaefer, V. Kempter, Electronic Structure of the Surface of the Ionic Liquid [EMIM][Tf$_2$N] Studied by Metastable Impact Electron Spectroscopy (MIES), UPS, and XPS, *Langmuir* **2006**, *22*, 7120-7123.

[63] K. Nakajima, S. Oshima, M. Suzuki, K. Kimura, Surface structures of equimolar mixtures of imidazolium-based ionic liquids using high-resolution Rutherford backscattering spectroscopy, *Surf. Sci.* **2012**, *606*, 1693-1699.

[64] K. Nakajima, S. Nakanishi, Z. Chval, M. Lísal, K. Kimura, Surface segregation in a binary mixture of ionic liquids: Comparison between high-resolution RBS measurements and molecular dynamics simulations, *J. Chem. Phys.* **2016**, *145*, 184704.

[65] S. Men, P. Licence, Probing the electronic environment of binary and ternary ionic liquid mixtures by X-ray photoelectron spectroscopy, *Chem. Phys. Lett.* **2017**, *686*, 74-77.

[66] I. J. Villar-Garcia, K. R. J. Lovelock, S. Men, P. Licence, Tuning the electronic environment of cations and anions using ionc liquid mixtures, *Chem. Sci.* **2014**, *5*, 2573-2579.

[67] S. Men, P. Licence, Tuning the electronic environment of the anion by using binary ionic liquid mixtures, *Chem. Phys. Lett.* **2017**, *681*, 40-43.

[68] E. J. Dick, A. E. A. Fouda, N. A. Besley, P. Licence, Probing the electronic structure of ether functionalised ionic liquids using X-ray photoelectron spectroscopy, *Phys. Chem. Chem. Phys.* **2020**, *22*, 1624-1631.

[69] S. Men, K. R. J. Lovelock, P. Licence, X-ray photoelectron spectroscopy of pyrrolidinium-based ionic liquids: cation–anion interactions and a comparison to imidazolium-based analogues, *Phys. Chem. Chem. Phys.* **2011**, *13*, 15244-15255.

[70] O. Hollóczki, M. Macchiagodena, H. Weber, M. Thomas, M. Brehm, A. Stark, O. Russina, A. Triolo, B. Kirchner, Triphilic Ionic-Liquid Mixtures: Fluorinated and Non-fluorinated Aprotic Ionic-Liquid Mixtures, *ChemPhysChem* **2015**, *16*, 3325-3333.

[71] A. Luís, K. Shimizu, J. M. M. Araújo, P. J. Carvalho, J. A. Lopes-da-Silva, J. N. Canongia Lopes, L. P. N. Rebelo, J. A. P. Coutinho, M. G. Freire, A. B. Pereiro, Influence of Nanosegregation on the Surface Tension of Fluorinated Ionic Liquids, *Langmuir* **2016**, *32*, 6130-6139.

[72]   D. Yang, F. Fu, L. Li, Z. Yang, Z. Wan, Y. Luo, N. Hu, X. Chen, G. Zeng, Unique orientations and rotational dynamics of a 1-butyl-3-methyl-imidazolium hexafluorophosphate ionic liquid at the gas–liquid interface: the effects of the hydrogen bond and hydrophobic interactions, *Phys. Chem. Chem. Phys.* **2018**, *20*, 12043-12052.

[73]   P. Wolf, M. Aubermann, M. Wolf, T. Bauer, D. Blaumeiser, R. Stepic, C. R. Wick, D. M. Smith, A.-S. Smith, P. Wasserscheid, J. Libuda, M. Haumann, Improving the performance of supported ionic liquid phase (SILP) catalysts for the ultra-low-temperature water–gas shift reaction using metal salt additives, *Green Chem.* **2019**, *21*, 5008-5018.

[74]   P. van der Heide, X-ray Photoelectron Spectroscopy: An Introduction to Principles and Practices, John Wiley & Sons, Inc., Hoboken, NJ, **2012**.

[75]   D. Briggs, M. P. Seah, Practical Surface Analysis: Volume 1 – Auger and X-ray Photoelectron Spectroscopy, 2nd Edition, John Wiley & Sons Ltd, Chichester, **1990**.

[76]   S. Hüfner, Photoelectron Spectroscopy: Principles and Applications, Third Edition, Springer-Verlag, Berlin, **2003**.

[77]   H. Hertz, Ueber einen Einfluss des ultravioletten Lichtes auf die electrische Entladung, *Ann. Phys.* **1887**, *267*, 983-1000.

[78]   W. Hallwachs, Ueber den Einfluss des Lichtes auf electrostatisch geladene Körper, *Ann. Phys.* **1888**, *269*, 301-312.

[79]   A. Einstein, Über einen die Erzeugung und Verwandlung des Lichtes betreffenden heuristischen Gesichtspunkt, *Ann. Phys.* **1905**, *322*, 132-148.

[80]   T. Cremer, M. Stark, A. Deyko, H.-P. Steinrück, F. Maier, Liquid/Solid Interface of Ultrathin Ionic Liquid Films: $[C_1C_1Im][Tf_2N]$ and $[C_8C_1Im][Tf_2N]$ on Au(111), *Langmuir* **2011**, *27*, 3662-3671.

[81]   S. Tanuma, C. J. Powell, D. R. Penn, Calculations of Electron Inelastic Mean Free Paths. V. Data for 14 Organic Compounds over the 50–2000 eV Range, *Surf. Interface Anal.* **1994**, *21*, 165-176.

[82]   T. Cremer, M. Killian, J. M. Gottfried, N. Paape, P. Wasserscheid, F. Maier, H.-P. Steinrück, Physical Vapor Deposition of [EMIM][Tf₂N]: A New Approach to the Modification ot Surface Properties with Ultrathin Ionic Liquid Films, *ChemPhysChem* **2008**, *9*, 2185-2190.

[83]   F. Rietzler, J. Nagengast, H.-P. Steinrück, F. Maier, Interface of Ionic Liquids and Carbon: Ultrathin $[C_1C_1Im][Tf_2N]$ Films on Graphite and Graphene, *J. Phys. Chem. C* **2015**, *119*, 28068-28076.

[84]   A. Deyko, T. Cremer, F. Rietzler, S. Perkin, L. Crowhurst, T. Welton, H.-P. Steinrück, F. Maier, Interfacial Behavior of Thin Ionic Liquid Films on Mica, *J. Phys. Chem. C* **2013**, *117*, 5101-5111.

[85]   Personal communication with J. N. Canongia Lopes and K. Shimizu, **2016**.

[86]   C. Kolbeck, J. Lehmann, K. R. J. Lovelock, T. Cremer, N. Paape, P. Wasserscheid, A. P. Fröba, F. Maier, H.-P. Steinrück, Density and Surface Tension of Ionic Liquids, *J. Phys. Chem. B* **2010**, *114*, 17025-17036.

[87] C. Kolbeck, T. Cremer, K. R. J. Lovelock, N. Paape, P. S. Schulz, P. Wasserscheid, F. Maier, H.-P. Steinrück, Influence of Different Anions on the Surface Composition of Ionic Liquids Studied Using ARXPS, *J. Phys. Chem. B* **2009**, *113*, 8682-8688.

[88] G. Laus, A. Schwärzler, P. Schuster, G. Bentivoglio, M. Hummel, K. Wurst, V. Kahlenberg, T. Lörting, J. Schütz, P. Peringer, G. Bonn, G. Nauer, H. Schottenberger, *N,N'*-Di(alkyloxy)imidazolium Salts: New Patent-free Ionic Liquids and NHC Precatalysts, *Z. Naturforsch.* **2007**, *62b*, 295-308.

[89] S. Bartz, B. Blumenröder, A. Kern, J. Fleckenstein, S. Frohnapfel, J. Schatz, A. Wagner, Hydroxy-1*H*-imidazole-3-oxides – Synthesis, Kinetic Acidity, and Application in Catalysis and Supramolecular Anion Recognition, *Z. Naturforsch.* **2009**, *64b*, 629-638.

[90] S. V. Dzyuba, R. A. Bartsch, Influence of Structural Variations in 1-Alkyl(aralkyl)-3-Methylimidazolium Hexafluorophosphates and Bis(trifluoromethylsulfonyl)-imides on Physical Properties of the Ionic Liquids, *ChemPhysChem* **2002**, *3*, 161-166.

[91] P. B. P. Serra, F. M. S. Ribeiro, M. A. A. Rocha, M. Fulem, K. Růžička, J. A. P. Coutinho, L. M. N. B. F. Santos, Solid-liquid equilibrium and heat capacity trend in the alkylimidazolium PF6 series, *J. Mol. Liq.* **2017**, *248*, 678-687.

[92] S. V. Dzyuba, R. A. Bartsch, New room-temperature ionic liquids with C_2-symmetrical imidazolium cations, *Chem. Commun.* **2001**, 1466-1467.

[93] C. P. Fredlake, J. M. Crosthwaite, D. G. Hert, S. N. V. K. Aki, J. F. Brennecke, Thermophysical Properties of Imidazolium-Based Ionic Liquids, *J. Chem. Eng. Data* **2004**, *49*, 954-964.

[94] H. Tokuda, K. Hayamizu, K. Ishii, M. A. B. H. Susan, M. Watanabe, Physicochemical Properties and Structures of Room Temperature Ionic Liquids. 1. Variation of Anionic Species, *J. Phys. Chem. B* **2004**, *108*, 16593-16600.

[95] H. Tokuda, K. Hayamizu, K. Ishii, M. A. B. H. Susan, M. Watanabe, Physicochemical Properties and Structures of Room Temperature Ionic Liquids. 2. Variation of Alkyl Chain Length in Imidazolium Cation, *J. Phys. Chem. B* **2005**, *109*, 6103-6110.

[96] B. S. J. Heller, C. Kolbeck, I. Niedermaier, S. Dommer, J. Schatz, P. Hunt, F. Maier, H.-P. Steinrück, Surface Enrichment in Equimolar Mixtures of Non-Functionalized and Functionalized Imidazolium-Based Ionic Liquids, *ChemPhysChem* **2018**, *19*, 1733-1745.

[97] I. Niedermaier, C. Kolbeck, H.-P. Steinrück, F. Maier, Dual analyzer system for surface analysis dedicated for angle-resolved photoelectron spectroscopy at liquid surfaces and interfaces, *Rev. Sci. Instrum.* **2016**, *87*, 045105.

[98] I. J. Villar-Garcia, E. F. Smith, A. W. Taylor, F. Qiu, K. R. J. Lovelock, R. G. Jones, P. Licence, Charging of ionic liquid surfaces under X-ray irradiation: the measurement of absolute binding energies by XPS, *Phys. Chem. Chem. Phys.* **2011**, *13*, 2797-2808.

[99] K. R. J. Lovelock, C. Kolbeck, T. Cremer, N. Paape, P. S. Schulz, P. Wasserscheid, F. Maier, H.-P. Steinrück, Influence of Different Substituents on the Surface

Composition of Ionic Liquids Studied Using ARXPS, *J. Phys. Chem. B* **2009**, *113*, 2854-2864.

[100] T. Cremer, Ionic Liquid Bulk and Interface Proberties: Electronic Interaction, Molecular Orientation and Growth Characteristics, Doctoral Thesis, Friedrich-Alexander-Universität Erlangen-Nürnberg, **2012**.

[101] C. Kolbeck, Surface Characterisation of Ionic Liquid Systems and *in situ* Monitoring of Liquid-Phase Reactions by X-ray Photoelectron Spectroscopy, Doctoral Thesis, Friedrich-Alexander-Universität Erlangen-Nürnberg, **2012**.

[102] I. Niedermaier, Surface Enrichment Effects, CO_2 Capture, and Acid-Base Reactions in Ionic Liquids Studied by Conventional and Dual Analyser X-ray Photoelectron Spectroscopy, Doctoral Thesis, Friedrich-Alexander-Universität Erlangen-Nürnberg, **2016**.

[103] F. Rietzler, Interfaces of Ionic Liquids and of Liquid Metals Studied by X-Ray Photoelectron Spectroscopy, Doctoral Thesis, Friedrich-Alexander-Universität Erlangen-Nürnberg, **2016**.

[104] I. Langmuir, The constitution and fundamental properties of solids and liquids. II. Liquids, *J. Am. Chem. Soc.* **1917**, *39*, 1848-1906.

[105] I. Langmuir, Forces Near the Surfaces of Molecules, *Chem. Rev.* **1930**, *6*, 451-479.

[106] K. Shimizu, B. S. J. Heller, F. Maier, H.-P. Steinrück, J. N. Canongia Lopes, Probing the Surface Tension of Ionic Liquids Using the Langmuir Principle, *Langmuir* **2018**, *34*, 4408-4416.

[107] C. Waring, P. A. J. Bagot, J. M. Slattery, M. L. Costen, K. G. McKendrick, $O(^3P)$ Atoms as a Probe of Surface Ordering in 1-Alkyl-3-methylimidazolium-Based Ionic Liquids, *J. Phys. Chem. Lett.* **2010**, *1*, 429-433.

[108] C. Waring, P. A. J. Bagot, J. M. Slattery, M. L. Costen, K. G. McKendrick, $O(^3P)$ Atoms as a Chemical Probe of Surface Ordering in Ionic Liquids, *J. Phys. Chem. A* **2010**, *114*, 4896-4904.

[109] M. A. Tesa-Serrate, B. C. Marshall, E. J. Smoll, Jr., S. M. Purcell, M. L. Costen, J. M. Slattery, T. K. Minton, K. G. McKendrick, Ionic Liquid–Vacuum Interfaces Probed by Reactive Atom Scattering: Influence of Alkyl Chain Length and Anion Volume, *J. Phys. Chem. C* **2015**, *119*, 5491-5505.

[110] S. Rivera-Rubero, S. Baldelli, Surface Characterization of 1-Butyl-3-methylimidazolium Br^-, I^-, PF_6^-, BF_4^-, $(CF_3SO_2)_2N^-$, SCN^-, $CH_3SO_3^-$, $CH_3SO_4^-$, and $(CN)_2N^-$ Ionic Liquids by Sum Frequency Generation, *J. Phys. Chem. B* **2006**, *110*, 4756-4765.

[111] C. S. Santos, S. Baldelli, Alkyl Chain Interaction at the Surface of Room Temperature Ionic Liquids: Systematic Variation of Alkyl Chain Length (R = C_1−C_4, C_8) in both Cation and Anion of [RMIM][R−OSO_3] by Sum Frequency Generation and Surface Tension, *J. Phys. Chem. B* **2009**, *113*, 923-933.

[112] S. Men, K. R. J. Lovelock, P. Licence, X-ray photoelectron spectroscopy of trihalide ionic liquids: Comparison to halide-based analogues, anion basicity and beam damage, *Chem. Phys. Lett.* **2017**, *679*, 207-211.

[113] B. May, M. Hönle, B. Heller, F. Greco, R. Bhuin, H.-P. Steinrück, F. Maier, Surface-Induced Changes in the Thermochromic Transformation of an Ionic Liquid Cobalt Thiocyanate Complex, *J. Phys. Chem. Lett.* **2017**, *8*, 1137-1141.

[114] C. Kolbeck, M. Killian, F. Maier, N. Paape, P. Wasserscheid, H.-P. Steinrück, Surface Characterization of Functionalized Imidazolium-Based Ionic Liquids, *Langmuir* **2008**, *24*, 9500-9507.

[115] C. J. Clarke, S. Maxwell-Hogg, E. F. Smith, R. R. Hawker, J. B. Harper, P. Licence, Resolving X-ray photoelectron spectra of ionic liquids with difference spectroscopy, *Phys. Chem. Chem. Phys.* **2019**, *21*, 114-123.

[116] T. Cremer, C. Kolbeck, K. R. J. Lovelock, N. Paape, R. Wölfel, P. S. Schulz, P. Wasserscheid, H. Weber, J. Thar, B. Kirchner, F. Maier, H.-P. Steinrück, Towards a Molecular Understanding of Cation–Anion Interactions—Probing the Electronic Structure of Imidazolium Ionic Liquids by NMR Spectroscopy, X-ray Photoelectron Spectroscopy and Theoretical Calculations, *Chem. Eur. J.* **2010**, *16*, 9018-9033.

[117] T. Hammer, M. Reichelt, H. Morgner, Influence of the aliphatic chain length of imidazolium based ionic liquids on the surface structure, *Phys. Chem. Chem. Phys.* **2010**, *12*, 11070-11080.

[118] R. M. Lynden-Bell, M. Del Pópolo, Simulation of the surface structure of butylmethylimidazolium ionic liquids, *Phys. Chem. Chem. Phys.* **2006**, *8*, 949-954.

[119] X. Paredes, J. Fernández, A. A. H. Pádua, P. Malfreyt, F. Malberg, B. Kirchner, A. S. Pensado, Using Molecular Simulation to Understand the Structure of $[C_2C_1im]^+$−Alkylsulfate Ionic Liquids: Bulk and Liquid−Vapor Interfaces, *J. Phys. Chem. B* **2012**, *116*, 14159-14170.

[120] A. S. Pensado, M. F. Costa Gomes, J. N. Canongia Lopes, P. Malfreyt, A. A. H. Pádua, Effect of alkyl chain length and hydroxyl group functionalization on the surface properties of imidazolium ionic liquids, *Phys. Chem. Chem. Phys.* **2011**, *13*, 13518-13526.

[121] A. S. Pensado, P. Malfreyt, A. A. H. Pádua, Molecular Dynamics Simulations of the Liquid Surface of the Ionic Liquid 1-Hexyl-3-methylimidazolium Bis(trifluoromethanesulfonyl)amide: Structure and Surface Tension, *J. Phys. Chem. B* **2009**, *113*, 14708-14718.

[122] R. M. Fogarty, R. Rowe, R. P. Matthews, M. T. Clough, C. R. Ashworth, A. Brandt, P. J. Corbett, R. G. Palgrave, E. F. Smith, R. A. Bourne, T. W. Chamberlain, P. B. J. Thompson, P. A. Hunt, K. R. J. Lovelock, Atomic charges of sulfur in ionic liquids: experiments and calculations, *Faraday Discuss.* **2018**, *206*, 183-201.

[123] G. Laus, A. Schwärzler, G. Bentivoglio, M. Hummel, V. Kahlenberg, K. Wurst, E. Kristeva, J. Schütz, H. Kopacka, C. Kreutz, G. Bonn, Y. Andriyko, G. Nauer, H. Schottenberger, Synthesis and Crystal Structures of 1-Alkoxy-3-alkylimidazolium Salts Including Ionic Liquids, 1-Alkylimidazole 3-oxides and 1-Alkylimidazole Perhydrates, *Z. Naturforsch.* **2008**, *63b*, 447-464.

[124] G. Laus, K. Wurst, V. Kahlenberg, H. Kopacka, C. Kreutz, H. Schottenberger, *N*-Heterocyclic Carbene (NHC) Derivatives of 1,3-Di(benzyloxy)imidazolium Salts, *Z. Naturforsch.* **2010**, *65b*, 776-782.

[125] A.-L. Revelli, F. Mutelet, J.-N. Jaubert, High Carbon Dioxide Solubilities in Imidazolium-Based Ionic Liquids and in Poly(ethylene glycol) Dimethyl Ether, *J. Phys. Chem. B* **2010**, *114*, 12908-12913.

[126] A.-L. Revelli, F. Mutelet, J.-N. Jaubert, Reducing of Nitrous Oxide Emissions Using Ionic Liquids, *J. Phys. Chem. B* **2010**, *114*, 8199-8206.

[127] Y. Deng, P. Besse-Hoggan, M. Sancelme, A.-M. Delort, P. Husson, M. F. Costa Gomes, Influence of oxygen functionalities on the environmental impact of imidazolium based ionic liquids, *J. Hazard. Mater.* **2011**, *198*, 165-174.

[128] C. Froschauer, R. Salchner, G. Laus, H. K. Weber, R. Tessadri, U. Griesser, K. Wurst, V. Kahlenberg, H. Schottenberger, 1,3-Di(alkoxy)imidazolium-based Ionic Liquids: Improved Synthesis and Crystal Structures, *Aust. J. Chem.* **2013**, *66*, 391-395.

[129] A. B. Pereiro, M. J. Pastoriza-Gallego, K. Shimizu, I. M. Marrucho, J. N. Canongia Lopes, M. M. Piñeiro, L. P. N. Rebelo, On the Formation of a Third, Nanostructured Domain in Ionic Liquids, *J. Phys. Chem. B* **2013**, *117*, 10826-10833.

[130] T. L. Merrigan, E. D. Bates, S. C. Dorman, J. H. Davis, Jr., New fluorous ionic liquids function as surfactants in conventional room-temperature ionic liquids, *Chem. Commun.* **2000**, 2051-2052.

[131] M. Tariq, M. G. Freire, B. Saramago, J. A. P. Coutinho, J. N. Canongia Lopes, L. P. N. Rebelo, Surface tension of ionic liquids and ionic liquid solutions, *Chem. Soc. Rev.* **2012**, *41*, 829-868.

[132] A. Dilks, The Identification of Peroxy-Features at Polymer Surfaces by ESCA, *J. Polym. Sci. Polym. Chem. Ed.* **1981**, *19*, 1319-1327.

[133] P. J. Carvalho, M. G. Freire, I. M. Marrucho, A. J. Queimada, J. A. P. Coutinho, Surface Tensions for the 1-Alkyl-3-methylimidazolium Bis(trifluoromethyl-sulfonyl)imide Ionic Liquids, *J. Chem. Eng. Data* **2008**, *53*, 1346-1350.

[134] T. M. Koller, M. H. Rausch, K. Pohako-Esko, P. Wasserscheid, A. P. Fröba, Surface Tension of Tricyanomethanide- and Tetracyanoborate-Based Imidazolium Ionic Liquids by Using the Pendant Drop Method, *J. Chem. Eng. Data* **2015**, *60*, 2665-2673.

[135] H. F. D. Almeida, M. G. Freire, A. M. Fernandes, J. A. Lopes-da-Silva, P. Morgado, K. Shimizu, E. J. M. Filipe, J. N. Canongia Lopes, L. M. N. B. F. Santos, J. A. P. Coutinho, Cation Alkyl Side Chain Length and Symmetry Effects on the Surface Tension of Ionic Liquids, *Langmuir* **2014**, *30*, 6408-6418.

[136] B. S. J. Heller, U. Paap, F. Maier, H.-P. Steinrück, Pronounced surface enrichment of fluorinated ionic liquids in binary mixtures with methoxy-functionalized ionic liquids, *J. Mol. Liq.* **2020**, *305*, 112783.

[137] B. S. J. Heller, M. Lexow, F. Greco, S. Shin, G. Partl, F. Maier, H.-P. Steinrück, Temperature-Dependent Surface Enrichment Effects in Binary Mixtures of Fluorinated and Non-Fluorinated Ionic Liquids, *Chem. Eur. J.* **2020**, *26*, 1117-1126.

[138] V. Lloret, M. Á. Rivero-Crespo, J. A. Vidal-Moya, S. Wild, A. Doménech-Carbó, B. S. J. Heller, S. Shin, H.-P. Steinrück, F. Maier, F. Hauke, M. Varela, A. Hirsch,

A. Leyva-Pérez, G. Abellán, Few layer 2D pnictogens catalyze the alkylation of soft nucleophiles with esters, *Nat. Commun.* **2019**, *10*, 509.

[139] E. F. Smith, I. J. Villar Garcia, D. Briggs, P. Licence, Ionic liquids *in vacuo*; solution-phase X-ray photoelectron spectroscopy, *Chem. Commun.* **2005**, 5633-5635.

[140] K. L. Kuntz, R. A. Wells, J. Hu, T. Yang, B. Dong, H. Guo, A. H. Woomer, D. L. Druffel, A. Alabanza, D. Tománek, S. C. Warren, Control of Surface and Edge Oxidation on Phosphorene, *ACS Appl. Mater. Interfaces* **2017**, *9*, 9126-9135.

8 Acknowledgment

9 Appendix

9.1 Publications [P1] – [P5]

[P1] **Probing the Surface Tension of Ionic Liquids Using the Langmuir Principle**

K. Shimizu, <u>B. S. J. Heller</u>, F. Maier, H.-P. Steinrück, J. N. Canongia Lopes

Langmuir **2018**, *34*, 4408–4416.

DOI: <u>10.1021/acs.langmuir.7b04237</u>

[P2] **Surface Enrichment in Equimolar Mixtures of Non-Functionalized and Functionalized Imidazolium-Based Ionic Liquids**

<u>B. S. J. Heller</u>, C. Kolbeck, I. Niedermaier, S. Dommer, J. Schatz, P. Hunt, F. Maier, H.-P. Steinrück

ChemPhysChem **2018**, *19*, 1733–1745.

DOI: <u>10.1002/cphc.201800216</u>

[P3] **Temperature-Dependent Surface Enrichment Effects in Binary Mixtures of Fluorinated and Non-Fluorinated Ionic Liquids**

<u>B. S. J. Heller</u>, M. Lexow, F. Greco, S. Shin, G. Partl, F. Maier, H.-P. Steinrück

Chem. Eur. J. **2020**, *26*, 1117–1126.

DOI: <u>10.1002/chem.201904438</u>

[P4] **Pronounced surface enrichment of fluorinated ionic liquids in binary mixtures with methoxy-functionalized ionic liquids**

B. S. J. Heller, U. Paap, F. Maier, H.-P. Steinrück

J. Mol. Liq. **2020**, *305*, 112783.

DOI: 10.1016/j.molliq.2020.112783

[P5] **Few layer 2D pnictogens catalyze the alkylation of soft nucleophiles with esters**

V. Lloret, M. Á. Rivero-Crespo, J. A. Vidal-Moya, S. Wild, A. Doménech-Carbó, B. S. J. Heller, S. Shin, H.-P. Steinrück, F. Maier, F. Hauke, M. Varela, A. Hirsch, A. Leyva-Pérez, G. Abellán

Nat. Commun. **2019**, *10*, 509.

DOI: 10.1038/s41467-018-08063-3

9.2 Unpublished Results

In the course of this thesis, investigations on several additional ILs have been carried out without being published. This chapter gives an overview of different classes of ILs, cleaning procedures applied and problems during investigation. An overview of the investigated ILs with their physical state at room temperature (RT) and some characteristics are given in Table 9.1.

All data presented in the appendix are depicted without any further data treatment, *i.e.* all binding energies are given as measured without any referencing. Only the 80° emission spectra are scaled up by the respective geometry factor[97] for a better visualization of enrichment and depletion effects occurring in the ILs.

Table 9.1: Overview of names, molecular structures and characteristics of supplementary ILs.

Short Name	IUPAC Name	Molecular Structure	Physical State at RT	Synthesized by	Remarks
[C$_8$AcIm]Cl	1-acetyl-3-octylimidazolium chloride		solid	M. Gantman	*d; Si;* no melting point
[C$_8$AcIm][PF$_6$]	1-acetyl-3-octylimidazolium hexafluorophosphate		solid	M. Gantman	*d, Si,* partly removed by sputtering and dissolving in solvent
[C$_8$AcIm][Tf$_2$N]	1-acetyl-3-octylimidazolium bis[(trifluoromethyl)sulfonyl]-imide		solid	M. Gantman	*d; Si*
[C$_4$(CO)C$_1$Im]Cl	1-methyl-3-valeroylimidazolium chloride		solid	M. Gantman	*d; Si*
[C$_4$(CO)C$_1$Im][Tf$_2$N]	1-methyl-3-valeroylimidazolium bis[(trifluoromethyl)sulfonyl]-imide		solid	M. Gantman	*d* before melting: *Si*
[C$_1$S(PFB)HIm][Tf$_2$N]	3-methyl-2-((3,3,4,4,4-penta-fluorobutyl)thio)imidazolium bis[(trifluoromethyl)sulfonyl]-imide		liquid	G. Partl	clean; not temperature stable; *dX* in mixture
[Ph$_3$PPhOPh][FAP]	(4-phenoxyphenyl)triphenyl-phosphonium tris(pentafluoro-ethyl)trifluorophosphate		liquid → solid	N. Taccardi	*Si; dX*
[Ph$_3$PPhOPh][Tf$_2$N]	(4-phenoxyphenyl)triphenyl-phosphonium bis[(trifluoro-methyl)sulfonyl]imide		liquid → solid	N. Taccardi	small *Si; dX*

d: decomposed IL measured (stoichiometry does not fit); *dX*: decomposition under X-rays; *Si*: polysiloxane contamination detected

145

9.2.1 (Pentafluorobutyl)thio-Functionalized Ionic Liquid and its Mixture with [C$_4$C$_1$Im][PF$_6$]

[C$_1$S(PFB)HIm][Tf$_2$N] was synthesized by Dr. Gabriel Partl as a yellow liquid at room temperature. Figure 9.1 shows the ARXP spectra in 0° (black) and 80° (red) emission of this protic IL at 24 °C.

No fitting constraints are applied except for the S 2p spin-orbit-split components (equal FWHM; area(p$_{3/2}$) = 2 · area(p$_{1/2}$); peak separation: 1.21 eV) and in the C 1s spectra the C$_{hetero'}$ peak is 1.1 times wider than the C$_2$ peak and both peaks are separated by 1.60 eV.

In 0° emission, one peak is detected in the O 1s spectrum as well as in the F 1s spectrum. The O$_{Tf2N}$ peak is located at 532.4 eV and the F$_{CFx}$ peak is at 688.5 eV consisting of several components which cannot be resolved with the DASSA setup: CF$_2$ and CF$_3$ groups of the fluorinated chain of the [C$_1$S(PFB)HIm]$^+$ cation and the CF$_3$ groups of the [Tf$_2$N]$^-$ anion. Two components are detected in the N 1s and S 2p spectra. The N$_{thio}$ and S$_{thio}$ peaks of the [C$_1$S(PFB)HIm]$^+$ cation are located at 401.6 and 165.2 eV. At 399.2 and 169.4 eV, the N$_{Tf2N}$ and S$_{Tf2N}$ peaks of the [Tf$_2$N]$^-$ anion are detected. Four peaks are detected in the C 1s spectrum. The C$_{hetero'}$, C$_2$, C$_{CF2}$ and C$_{CF3}$ peaks are at 286.2, 287.8, 290.8 and 292.8 eV, respectively. Like in the F$_{CFx}$ peak, signals of the CF$_3$ group of the fluorinated chain of the [C$_1$S(PFB)HIm]$^+$ cation and the CF$_3$ groups of the [Tf$_2$N]$^-$ anion are overlapping in the C$_{CF3}$ peak. No signal is detected in the Si 2p region confirming a high purity of the IL as polysiloxane from *e.g.* glass ware or septa is a common contamination in ILs.[47, 139] The quantitative analysis, given in Table 9.2, shows also a good agreement between the atom numbers in 0° emission and the nominally expected numbers.

In 80° emission (red in Figure 9.1), the O$_{Tf2N}$, N$_{Tf2N}$ and S$_{Tf2N}$ signals are lower in intensity compared to 0° indicating a depletion of these atoms of the [Tf$_2$N]$^-$ anion whereas the intensity of the C$_{CF2}$, C$_{CF3}$ and F$_{CFx}$ peaks is the same or even higher in 80° compared to 0° suggesting that the CF$_3$ groups of the anion are pointing towards the vacuum as well as the fluorinated chain of the [C$_1$S(PFB)HIm]$^+$ cation.
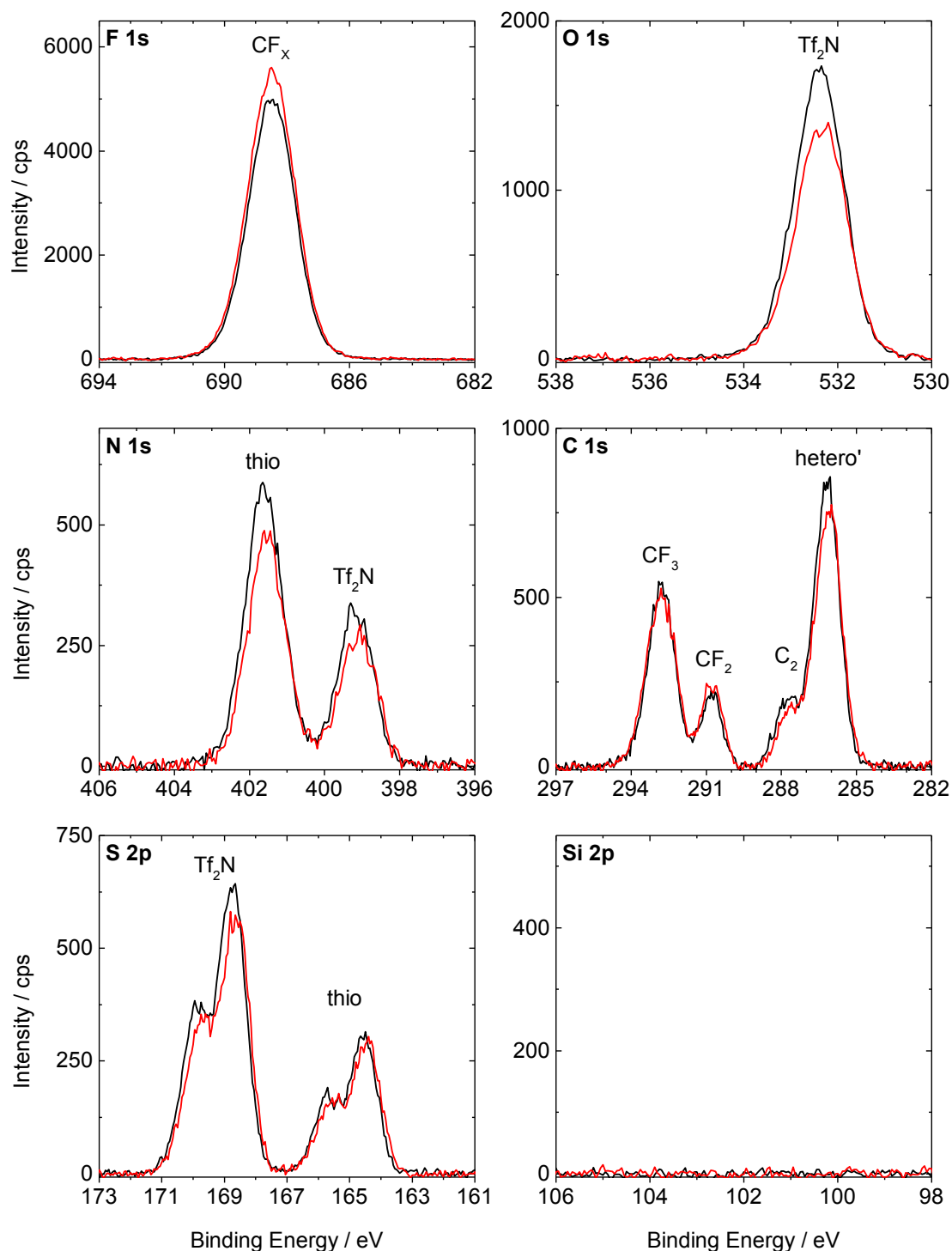
Figure 9.1: ARXP spectra of [C_1S(PFB)HIm][Tf_2N] in 0° (black) and 80° (red) emission recorded at 24 °C.

The aim of the measurements of [C_1S(PFB)HIm][Tf_2N] was to test its suitability as second example of a fluorinated IL in mixtures to perform similar experiments as described in Chapter 4.2.2 for mixtures of [PFBMIm][PF_6] and [$C_n C_1$Im][PF_6]. Measurements at elevated temperature result in a strong decrease of the cation related signals

indicating the decomposition of the $[C_1S(PFB)HIm]^+$ cation. In addition, a peak broadening of the $[Tf_2N]^-$ anion signals is detected. Also an influence of the X-rays on the decomposition of the IL cannot be ruled out.

Table 9.2: Quantitative analysis of the 0° and 80° XP spectra of $[C_1S(PFB)HIm][Tf_2N]$ at 24 °C.

	F 1s	O 1s	N 1s		C 1s				S 2p	
	CFx	Tf₂N	thio	Tf₂N	CF₃	CF₂	C₂	hetero'	Tf₂N	thio
Binding Energy / eV	688.5	532.4	401.6	399.2	292.8	290.8	287.8	286.2	169.4	165.2
ASF	1.00	0.67	0.46	0.46	0.30	0.30	0.30	0.30	0.64	0.64
Nominal	*11*	*4*	*2*	*1*	*3*	*1*	*1*	*5*	*2*	*1*
0° emission	11.54	4.21	1.97	1.04	3.00	0.89	0.91	4.42	2.07	0.95
80° emission	12.93	3.55	1.64	0.91	3.16	1.01	0.79	4.17	1.91	0.93

Additionally, an equimolar mixture of $[C_1S(PFB)HIm][Tf_2N]$ and $[C_4C_1Im][PF_6]$ was prepared. To ensure proper mixing of both ILs, acetone (Sigma-Aldrich, purity $\geq 99.5\%$) was used as a co-solvent. The solution was spread on a molybdenum sample holder and the solvent acetone evaporated at RT due to the previously described decomposition of the $[C_1S(PFB)HIm]^+$ cation at higher temperatures.

The ARXP spectra recorded at 24 °C are presented in Figure 9.2. In 0° (black) emission, the signals of the $[PF_6]^-$ anion, F_{PF6} and P_{PF6}, are at 686.5 and 136.8 eV, respectively. The O_{Tf2N}, N_{Tf2N} and S_{Tf2N} signals of the other anion are located at 532.5, 399.3 and 169.4 eV, respectively. As mentioned above for neat $[C_1S(PFB)HIm][Tf_2N]$, the XP peaks of the CF_3 group of the fluorinated chain in the cation and the CF_3 groups of the $[Tf_2N]^-$ anion are superimposed (F_{CFx} at 688.6 eV and C_{CF3} at 292.9 eV). In addition to the CF_3 signal of the $[C_1S(PFB)HIm]^+$ cation, the C_{CF2}, $C_{2,thio}$ and $C_{hetero',thio}$ peaks are located at 290.9, 287.8 and 286.2 eV, respectively, in the C 1s spectrum. The signals of the $[C_4C_1Im]^+$ cation are at 287.4, 286.5 and 284.9 eV for the $C_{2,C4C1}$, $C_{hetero',C4C1}$ and C_{alkyl}, respectively. Note that as a fit model the constraints for both neat ILs are applied for fitting the C 1s spectrum without any sophisticated optimization. In the N 1s spectrum, the signal of the nitrogen atoms of the imidazolium ring of the $[C_1S(PFB)HIm]^+$ cation, N_{thio}, cannot be distinguished from the signal of the nitrogen atoms of the $[C_4C_1Im]^+$ imidazolium ring, N_{C4C1}, resulting in a combined peak at 401.8 eV. The S_{thio} peak is located at 165.2 eV. No Si 2p or other XP signals are detected in addition to the expected IL mixture signals confirming that no contaminations are transferred into the mixture during sample

preparation. Within the margin of error, the quantitative analysis (see Table 9.3) in 0° emission fits with the nominal atom ratio.

To get information about the surface enrichment and depletion effects in the equimolar mixture of $[C_1S(PFB)HIm][Tf_2N]$ and $[C_4C_1Im][PF_6]$ the 80° (red) spectra are analyzed (see Figure 9.2). The intensity in 0° and 80° emission is roughly the same for the O_{Tf2N}, N_{Tf2N} and S_{Tf2N} signals of the $[Tf_2N]^-$ anion while the F_{PF6} and P_{PF6} peaks of the $[PF_6]^-$ anion have a lower intensity in 80° than in 0°, indicating a depletion of the $[PF_6]^-$ anion with respect to the $[Tf_2N]^-$ anion as known from literature.[61, 63, 96] The F_{CFx}, C_{CF3} and C_{CF2} intensities are higher in 80° emission indicating a surface enrichment of the fluorinated chain of the $[C_1S(PFB)HIm]^+$ cation and the $[Tf_2N]^-$ anion. This enrichment is more pronounced in contrast to neat $[C_1S(PFB)HIm][Tf_2N]$. No changes in intensity are detected for the S_{thio} peak when changing the emission angle. Due to the S_{thio} signal and the intensity decrease of the combined N_{C4C1} and N_{thio} peak from 80° emission to 0° most likely the head group of the $[C_4C_1Im]^+$ cation is depleted from the surface compared to the surface-enriched head group of the $[C_1S(PFB)HIm]^+$ cation. In the C 1s region, the signal between 285 and 289 eV has also a lower intensity in 80° but it is hard to say anything about the relative positions of the two head groups with respect to each other. As mentioned, the fitting model preliminary used for the C 1s spectrum does not allow for reliable quantitative ARXPS analysis.

Since neat $[C_1S(PFB)HIm][Tf_2N]$ decomposes at elevated temperature, a cooling experiment starting from RT was performed. The decomposition of the $[C_1S(PFB)HIm]^+$ cation and a third F 1s species appearing at ~684.7 eV are detected. Presumably, the extended X-ray exposure time destroys the mixture due to a limited diffusion of the molecules.
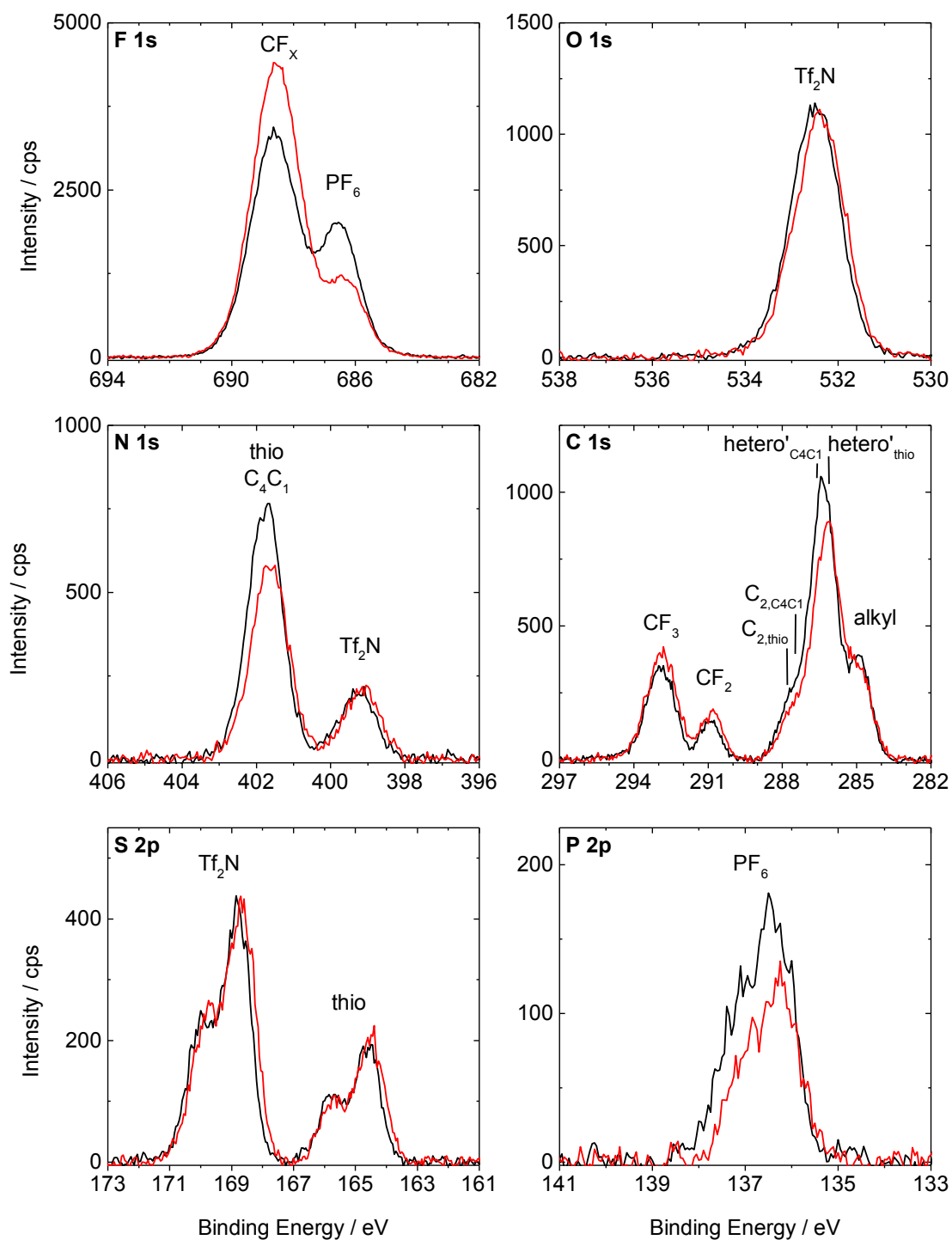
Figure 9.2: ARXP spectra of an equimolar mixture of [C$_1$S(PFB)HIm][Tf$_2$N] and [C$_4$C$_1$Im][PF$_6$] in 0° (black) and 80° (red) emission recorded at 24 °C.

Table 9.3: Quantitative analysis of the 0° and 80° XP spectra of an equimolar mixture of $[C_1S(PFB)HIm][Tf_2N]$ and $[C_4C_1Im][PF_6]$ at 24 °C.

| | F 1s | | O 1s | N 1s | | C 1s | | | | | | | S 2p | | P 2p |
| | | | | | | $[C_1S(PFB)HIm]^+$ (thio) | | | | $[C_4C_1Im]^+$ | | | | | |
	CF_x	PF_6	Tf_2N	thio	Tf_2N	CF_3	CF_2	C_2	hetero'	C_2	hetero'	alkyl	Tf_2N	thio	PF_6
Binding Energy / eV	688.6	686.5	532.5	401.8	399.3	292.9	290.9	287.8	286.2	287.4	286.5	284.9	169.4	165.2	136.8
ASF	1.00	1.00	0.67	0.46	0.46	0.30	0.30	0.30	0.30	0.30	0.30	03.0	0.64	0.64	0.46
Nominal	*11*	*6*	*4*	*4*	*1*	*3*	*1*	*1*	*5*	*1*	*4*	*3*	*2*	*1*	*1*
0° emission	12.23	5.78	4.32	3.76	1.05	3.23	0.89	0.89	4.66	0.89	3.54	2.72	2.07	0.91	1.07
80° emission	16.32	3.14	4.22	3.07	1.08	3.90	1.18	0.92	3.66	0.92	3.66	2.56	2.19	0.97	0.73

9.2.2 Ether-Functionalized Phosphonium Ionic Liquids

[Ph$_3$PPhOPh][FAP] and [Ph$_3$PPhOPh][Tf$_2$N] were synthesized by Dr. Nicola Taccardi as yellow, very viscous liquids (at RT) which crystalized over time becoming white solids. T_m is ~75 °C for [Ph$_3$PPhOPh][FAP] and ~91 °C for [Ph$_3$PPhOPh][Tf$_2$N] (both temperatures are deduced from samples heated up in the preparation chamber of the DASSA setup). The samples were measured at 105 °C in their liquid state.

No fitting constraints are applied except for the S 2p and P 2p spin-orbit-split components (equal FWHM; area(p$_{3/2}$) = 2 · area(p$_{1/2}$); peak separation S 2p = 1.21 eV, P 2p = 0.90 eV). For determining the atom numbers in 0° and 80° emission, the C$_{CF3}$ and C$_{CF2}$ peak intensities are linked to the F$_{CFx}$ peak. The remaining shake-up intensity between 288 and 294 eV in the C 1s region is added to the intensity of the C$_{phenyl}$ peak. The quantitative analyses are provided in Table 9.4.

Table 9.4: Quantitative analysis of the 0° and 80° XP spectra of a) [Ph$_3$PPhOPh][FAP] and b) [Ph$_3$PPhOPh][Tf$_2$N] at 105 °C.

a) [Ph$_3$PPhOPh][FAP]	F 1s	O 1s		C 1s				P 2p	
	CF$_x$	P-F	C-O-C	CF$_3$	CF$_2$	C-O-C	contami-nation + phenyl	FAP	cation
Binding Energy / eV	687.9	686.2	533.5	292.7	289.6	286.7	285.0	134.7	133.3
ASF	1.00	1.00	0.67	0.30	0.30	0.30	0.30	0.46	0.46
Nominal	*15*	*3*	*1*	*3*	*3*	*2*	*28*	*1*	*1*
0° emission	14.44	2.81	1.02	2.89	2.89	1.21	29.80	1.02	0.91
80° emission	8.93	1.66	1.08	1.79	1.79	0.63	39.62	0.81	0.70

b) [Ph$_3$PPhOPh][Tf$_2$N]	F 1s	O 1s		N 1s	C 1s			S 2p	P 2p
	Tf$_2$N	C-O-C	Tf$_2$N	Tf$_2$N	Tf$_2$N	C-O-C	phenyl	Tf$_2$N	cation
Binding Energy / eV	688.7	533.7	532.4	399.2	292.7	286.8	285.3	169.4	133.6
ASF	1.00	0.67	0.67	0.46	0.30	0.30	0.30	0.64	0.46
Nominal	*6*	*1*	*4*	*1*	*2*	*2*	*28*	*2*	*1*
0° emission	6.24	1.11	4.12	1.04	2.08	1.91	27.52	2.05	0.93
80° emission	6.53	1.11	3.95	0.99	2.18	1.78	27.61	1.97	0.87

In general, [Ph₃PPhOPh][FAP] (see Figure 9.3) has a strong surface active contamination which is presumably polysiloxane whereas for [Ph₃PPhOPh][Tf₂N] (see Figure 9.4) only a very small contamination in the Si 2p region (not shown) is observed. A homogeneous distribution of all moieties of [Ph₃PPhOPh][Tf₂N] is detected. Both ILs are decomposing under X-rays within a few hours as indicated by peak broadening.
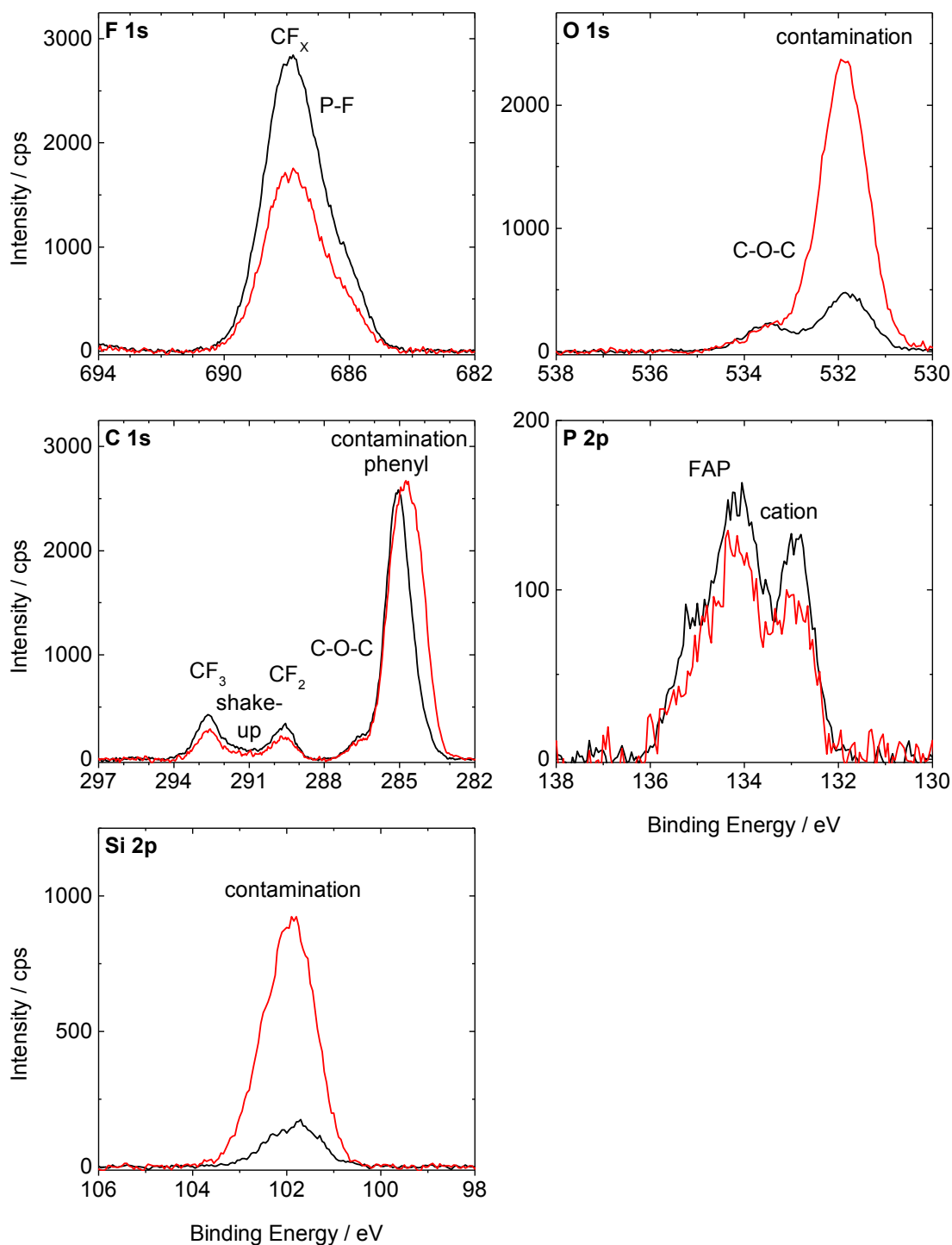
Figure 9.3: ARXP spectra of [Ph₃PPhOPh][FAP] in 0° (black) and 80° (red) emission recorded at 105 °C.
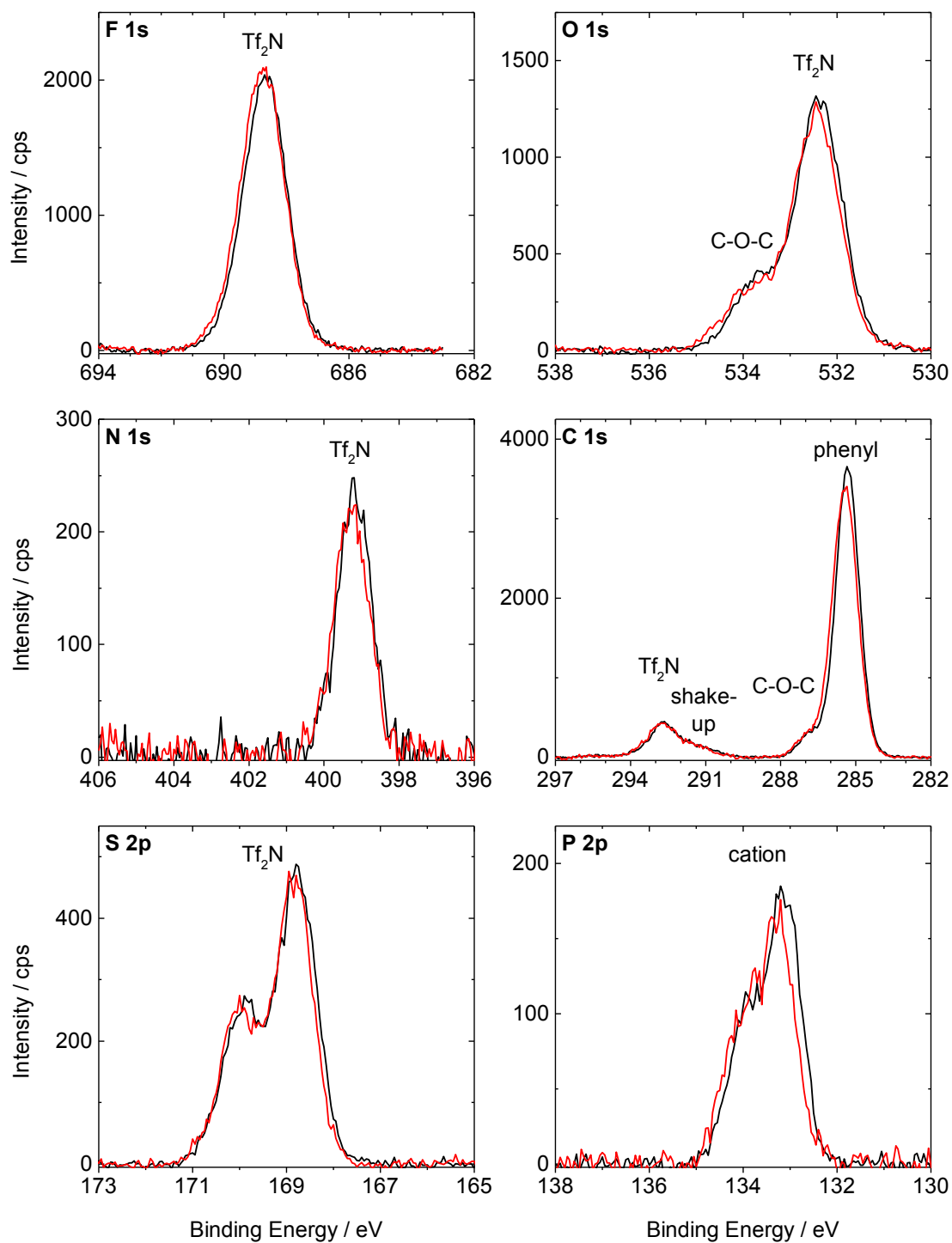
Figure 9.4: ARXP spectra of [Ph$_3$PPhOPh][Tf$_2$N] in 0° (black) and 80° (red) emission recorded at 105 °C.

9.2.3 Temperature-Dependent Measurements of Mixtures of [PFBMIm][PF$_6$] with [C$_2$C$_1$Im][PF$_6$] and [C$_8$C$_1$Im][PF$_6$]

As highlighted in Chapter 4.2.2, temperature-dependent ARXPS measurements of mixtures of [PFBMIm][PF$_6$] and [C$_2$C$_1$Im][PF$_6$] or [C$_8$C$_1$Im][PF$_6$] were investigated besides the published measurements of mixtures containing [PFBMIm][PF$_6$] and [C$_4$C$_1$Im][PF$_6$].[137] For the data of all these mixtures, the published fitting constraints are applied.[137]

The ARXP spectra of [C$_2$C$_1$Im][PF$_6$] recorded at 95 °C show the expected peaks in the F 1s, N 1s, C 1s and P 2p regions in 0° and 80° emission. In addition, a polysiloxane contamination is detected in the O 1s and Si 2p spectra as well as a too high C$_{alkyl}$ peak in the C 1s region as deduced from the quantitative analysis and the 80° spectrum.

When preparing mixtures of [PFBMIm][PF$_6$] and [C$_2$C$_1$Im][PF$_6$] with 10, 25, 50 and 75 mol% [PFBMIm][PF$_6$], a cleaning procedure is applied. Both solids are dissolved in acetonitrile. Subsequently, only the lower part of the solution is carefully extracted with a Pasteur pipette, assuming that most of the surface-enriched polysiloxane contamination stays in the remaining topmost 1 to 2 mm of the solution. Unfortunately, this cleaning process has not led to the intended outcome of contamination free samples as illustrated in the 80° survey spectrum of a mixture containing 10 mol% [PFBMIm][PF$_6$] in Figure 9.5–I measured at 95 °C. In contrast to the spectrum of neat [C$_2$C$_1$Im][PF$_6$], no Si contamination peak is observed but an oxygen peak as well as a dominating C 1s signal are visible in ARXPS while the IL peaks are very weak. Furthermore, a dewetting of the 10, 25 and 50 mol% [PFBMIm][PF$_6$] mixtures on the molybdenum sample holder is visually observed as well as the XP spectra reveal additional Mo signals.

Gentle sputtering with 300 eV Ar$^+$ ions (~8 µA) for 5 to 15 min improves the wetting on the sample holder for the 10, 25 and 50 mol% [PFBMIm][PF$_6$] mixtures. This is attributed to the removal of some contamination on the molybdenum sample holder by sputtering. In Figure 9.5–II, the survey spectrum of the 10 mol% [PFBMIm][PF$_6$] mixture after the sputter process indicates not only the improvement of the wetting behavior by the absence of the Mo and O 1s signals but also shows strong IL signals. Note that for the 75 mol% [PFBMIm][PF$_6$] mixture no dewetting and no oxygen, silicon and carbon contaminations are observed.
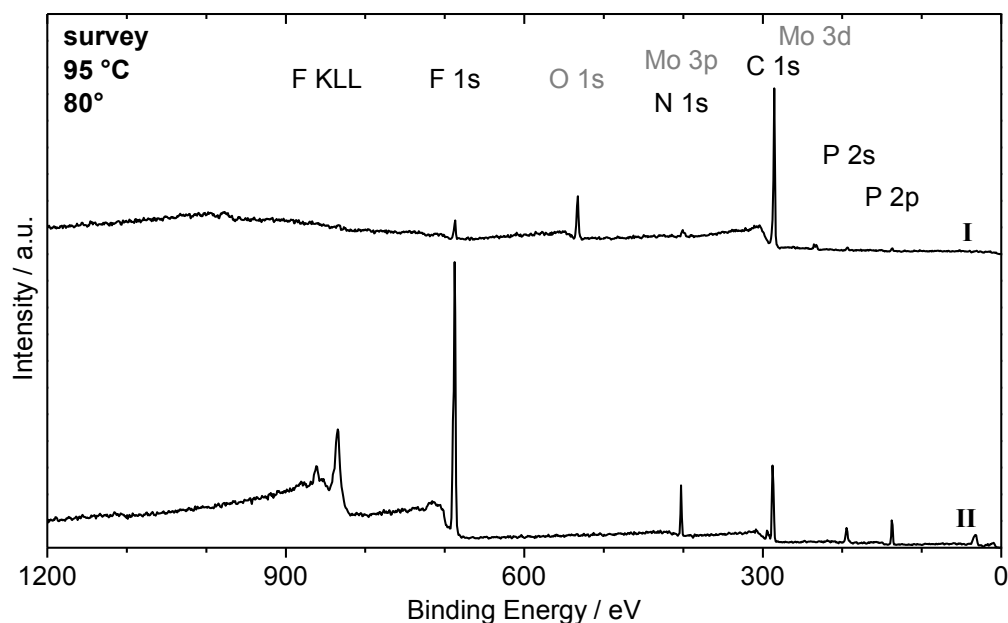
Figure 9.5: Survey spectra of a 10 mol% mixture of [PFBMIm][PF$_6$] and [C$_2$C$_1$Im][PF$_6$] as prepared (I) and after sputtering (II) recorded at an emission angle of 80°. The sample temperature was 95 °C. The spectra are offset for clarity.

In addition, mixtures of [PFBMIm][PF$_6$] and [C$_8$C$_1$Im][PF$_6$] with 10, 25, 50 and 75 mol% [PFBMIm][PF$_6$] are prepared using acetonitrile as a co-solvent. No further treatment is necessary because these mixtures fully wet the sample holders and no contamination is detected in the ARXP spectra. For the 10 mol% mixture of [PFBMIm][PF$_6$] and [C$_8$C$_1$Im][PF$_6$], an additional FWHM constraint is applied: The F$_{PF6}$ peak is 0.76 times wider than the F$_{CFx}$ peak due to a dominating F$_{PF6}$ peak in the F 1s spectra.

All mixtures are measured at 95 °C and subsequently cooled to lower temperature until peak broadening or shifts are detected indicating the onset of solidification. In general, the same trends, *e.g.* the surface enrichment of the fluorinated chain of the [PFBMIm]$^+$ cation in contrast to the surface-depleted [PF$_6$]$^-$ anion, are observed as described for the mixtures of [PFBMIm][PF$_6$] and [C$_4$C$_1$Im][PF$_6$] in Chapter 4.2.2. This is attributed to the difference in surface tension of the [C$_n$C$_1$Im][PF$_6$] and the [PFBMIm][PF$_6$] as it is in accordance with literature that ILs containing fluorinated chains generally possess a lower surface tension compared to their alkylated counterpart[60, 130, 131] and the shorter the alkyl chain, the higher is the surface tension of the IL.[71, 86, 133-135]

At 95 °C, a more pronounced enrichment of the fluorinated chain of the [PFBMIm]$^+$ cation relative to the [PF$_6$]$^-$ anion is detected in the F 1s spectrum for both

types of mixtures when decreasing the [PFBMIm][PF$_6$] content. This is visualized in Figure 9.6 by plotting the normalized ratio of the F_{CFx} and F_{PF6} intensities for the mixtures containing [C$_2$C$_1$Im][PF$_6$] (blue triangles) and [C$_8$C$_1$Im][PF$_6$] (green diamonds) in 0° (open symbols) and 80° (full symbols) emission. The enrichment of the fluorinated chain of the [PFBMIm]$^+$ cation is also detected by the intensity increase of the C_{CF3} and C_{CF2} peaks in the C 1s spectrum of the mixtures when comparing the 0° and 80° spectra. Another observation is that in 80° the enrichment is much less pronounced for the mixtures with [C$_8$C$_1$Im][PF$_6$] compared to the mixtures containing [C$_2$C$_1$Im][PF$_6$] which is attributed to a competing effect of the fluorinated chain and the longer alkyl chain.[71] In 0° emission, even the same trend is observed but to a lower extent than in 80°, revealing that below the first 1 to 1.5 nm an enrichment of the fluorinated chain of the [PFBMIm]$^+$ cation is detected as observed for other IL systems as well.[54, 96, 136, 137]
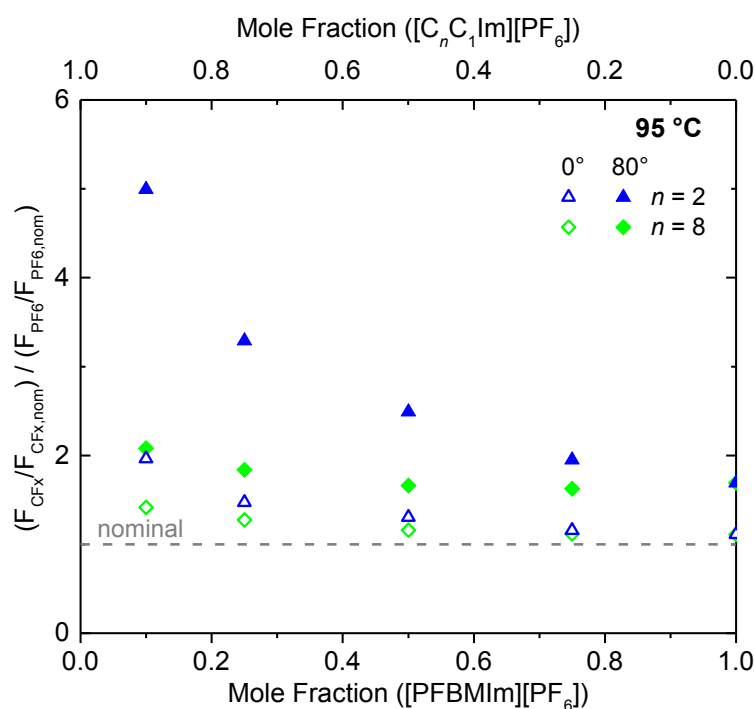
Figure 9.6: Normalized ratio of F_{CFx} and F_{PF6} for mixtures of [PFBMIm][PF$_6$] and [C$_n$C$_1$Im][PF$_6$] with $n = 2$ (blue triangles) and 8 (green diamonds) at 0° (open symbols) and 80° (full symbols) emission. The gray dashed line indicates the nominal composition. The sample temperature was 95 °C.

Furthermore, the C_{alkyl} signal in the C 1s spectra of the mixtures of [PFBMIm][PF$_6$] and [C$_8$C$_1$Im][PF$_6$] has a higher intensity in 80° compared to 0° emission showing the surface enrichment of the octyl chain of the [C$_8$C$_1$Im]$^+$ cation besides the enrichment of the fluorinated chain of the [PFBMIm]$^+$ cation. This is in contrast to the mixtures containing

$[C_2C_1Im][PF_6]$ and $[C_4C_1Im][PF_6]$ for which no enrichment of the alkyl chain is detected. This observation is in line with MD simulations of Luís *et al.*[71] indicating that the surface of mixtures, containing long alkyl chains and shorter fluorinated chains, is dominated by the alkyl chains. This is on expense of the shorter fluorinated chain and the cationic head groups, whereas in the presence of a short alkyl chain the surface is dominated by the fluorinated chain.

For the temperature-dependent measurements, only the 80° emission spectra of the mixtures of $[PFBMIm][PF_6]$ and $[C_2C_1Im][PF_6]$ or $[C_8C_1Im][PF_6]$ are briefly discussed because the enrichment and depletion effects are more obvious under this emission angle. When decreasing the temperature, the signals of the fluorinated chain, F_{CFx}, C_{CF3} and C_{CF2}, increase in intensity whereas the F_{PF6} peak intensity decreases. In the XP spectra of the mixtures containing $[C_8C_1Im][PF_6]$, the C_{alkyl} signal increases as well. Figure 4.6 in Chapter 4.2.2 shows the increase of the normalized intensity ratio of F_{CFx} and F_{PF6} of the mixtures of $[PFBMIm][PF_6]$ and $[C_nC_1Im][PF_6]$ with $n = 2$ (blue triangles), 4 (red squares) and 8 (green diamonds) with decreasing temperature indicating a more pronounced surface enrichment of the fluorinated chain of the $[PFBMIm]^+$ cation with respect to the $[PF_6]^-$ anion relative to the bulk concentration.

In general, the most pronounced surface enrichment of the fluorinated chain of the $[PFBMIm]^+$ cation is detected for the mixtures containing $[PFBMIm][PF_6]$ and $[C_2C_1Im][PF_6]$ compared to the mixtures of $[PFBMIm][PF_6]$ with $[C_4C_1Im][PF_6]$ or $[C_8C_1Im][PF_6]$ and this effect is enhanced when decreasing the temperature.